

Supplementary Information

Isotropically conducting tetraaryl osmium(IV), silane, and methane molecular wire junctions

Luana Zagami,^a Cynthia Avedian,^a Mukund Sharma,^a Andrew Fraire,^a Clarissa Olivar,^a Thomas M. Czyszczon-Burton,^a Daniel Hernangómez-Pérez,^{b,*} and Michael S. Inkpen^{a,*}

^a Department of Chemistry, University of Southern California, Los Angeles, CA 90089, USA

^b CIC nanoGUNE BRTA, Tolosa Hiribidea, 76, 20018 Donostia-San Sebastián, Spain

E-mail: d.hernangomez@nanogune.eu, inkpen@usc.edu

Contents

1. General Information	S2
2. Synthetic Details	S7
3. Electrochemistry	S12
4. UV-Vis Spectroscopy	S13
5. Additional Conductance Data	S15
6. Additional Computational Data	S26
7. NMR Spectra	S39
8. References	S45

1. General Information

Synthetic Methods

Manipulations under a nitrogen atmosphere were carried out in oven-dried glassware using standard Schlenk line techniques. No special precautions were taken to exclude air or moisture during workup unless otherwise stated. Tetrahydrofuran (THF) was sparged with nitrogen and dried using a two-column solvent purification system packed with alumina (Pure Process Technologies, Nashua, NH, USA). N,N-Dimethylformamide (DMF) was purified by vacuum distillation, dried over 3 Å molecular sieves,¹ and stored under nitrogen. Molecular sieves were activated by heating for ≥3.5 h at 350°C in a muffle furnace (Thermolyne, Thermo Scientific, Asheville, NC, USA), and stored in a desiccator until use. Grignard reagents were commercially available, or prepared according to the general method described in previous literature,² and titrated using a salicylaldehyde phenylhydrazone indicator to determine their concentration prior to use.³ (Oct₄N)₂[OsBr₆]² tetrakis(4-bromo-2,5-dimethylphenyl)osmium(IV),⁴ tetrakis(2,5-dimethyl-4-(methylthio)phenyl)osmium(IV) (**Os1**),⁵ tetrakis(4-bromophenyl)silane,⁶ and (4'-(methylthio)-[1,1'-biphenyl]-4-yl)(triphenylphosphine)gold(I) (**Au2**)⁷ were prepared using established literature procedures. Other reaction solvents (sparged with nitrogen prior to use) and chemical reagents were commercially available and used without further purification. 18.2 MΩ water was generated using an Arium® Mini Plus UV ultrapure water system (Sartorius AG, Goettingen, Germany). Deuterated solvents were purchased from Cambridge Isotope Laboratories, Inc., Cambridge Isotope Laboratories, Tewksbury, MA USA. Flash chromatography was performed using a Pure C-850 FlashPrep chromatography system and FlashPure EcoFlex flash cartridges (silica, irregular 50-75 μm particle size, 50-70 Å pore size; BUCHI Corporation, New Castle, DE, USA). Reaction yields are unoptimized.

¹H and ¹³C{¹H} NMR spectra were recorded at room temperature on Varian VNMRS 500 (500 MHz), VNMRS 400 (400 MHz), or Mercury 400 (400 MHz) NMR spectrometers. ¹H NMR data recorded in CDCl₃ and CD₂Cl₂ is referenced to residual internal CHCl₃ (δ 7.26) and CH₂Cl₂ (δ 5.32) solvent signals.⁸ ¹³C{¹H} NMR data recorded in CDCl₃ and CD₂Cl₂ is referenced to internal CDCl₃ (δ 77.16) and CD₂Cl₂ (δ 53.52).⁸ ¹H and ¹³C{¹H} resonances were assigned where possible for new compounds using 2D correlation spectroscopy experiments. UV-vis spectra were obtained with 0.1 mM solutions in a 10 mm/1 mm pathlength quartz cell (Starna Cells, Starna

Cells, Inc., Atascadero, CA, USA), using a Cary 60 UV-vis Spectrophotometer (Agilent Technologies, Inc., Santa Clara, CA, USA) or an AvaSpec-ULS2048-EVO UV/vis Spectrometer integrated with an AvaLight UV/vis/NIR Light Source (Pine Research Instrumentation, Durham, NC, USA; Avantes North America, Lafayette, CO, USA). Mass spectrometry analyses were performed on a Waters GCT Premier (EI), JEOL Accu-TOF JMS-T2000GC (EI), Waters Synapt G2-Si (ESI), Bruker Autoflex Speed LRF (MALDI), or Bruker Daltonics UltrafleXtreme (MALDI) at the Mass Spectrometry Lab, University of Illinois Urbana-Champaign.

Scanning Tunneling Microscope-based Break Junction (STM-BJ)

These details are reproduced here from a previous report, with only minor changes, for convenience.⁹ STM–BJ measurements were performed using custom-built setups that have been described previously,^{10–12} operated in ambient atmosphere at room temperature. Hardware was controlled and analyses were performed using custom software (written using IgorPro, Wavemetrics Inc., OR, USA). Tip–substrate distances were controlled with sub-angstrom precision using a single-axis preloaded piezoelectric actuator (P-840.1, Physik Instrumente, MA, USA). Tunneling currents were measured using a DLPCA-200 variable gain low noise transimpedance current amplifier (FEMTO Messtechnik GmbH, Berlin, Germany). Applying a bias between the tip and substrate, conductance was measured as a function of tip–substrate displacement (at 40 kHz acquisition rate) as the tip was repeatedly pushed into the substrate to reach a conductance of $>5 G_0$ (where $G_0 = 2e^2/h$) and then retracted 5–10 nm (at 20 nm/s) to break the contact. The resulting conductance-distance traces were compiled into 1D conductance histograms (using 100 bins/decade along the conductance axis), or 2D conductance-distance histograms (using 100 bins/decade along the conductance axis and 1000 bins/nm along the displacement axis). Traces in 2D histograms were aligned such that displacement = 0 nm where $G = 0.5 G_0$. Color scales inset in 2D histograms are in count/1000 traces. Most probable conductance values for molecules studied here were obtained through Gaussian fits to their corresponding conductance peaks in 1D histograms. All histograms were constructed from $\geq 5,000$ traces, unless otherwise stated.

STM tips were prepared from freshly cut Au wire ($\varnothing = 0.25$ mm; 99.998%, Alfa Aesar, MA, USA or 99.999%, Beantown Chemical, NH, USA). Substrates were prepared from evaporation of 100–200 nm Au (99.9985%, Alfa Aesar, or 99.999%, Angstrom Engineering Inc., ON, Canada) at a rate of $\sim 1 \text{ \AA/s}$ onto mechanically polished AFM/STM steel specimen discs (Ted

Pella Inc., CA, USA) with a COVAP Physical Vapor Deposition System (Angstrom Engineering Inc.) used exclusively for metal evaporation. Gold substrates were UV-ozone cleaned (Probe and Surface Decontamination Standard System, Novascan Technologies, Inc., IA, USA) and used for measurements that same day. Directly before starting a solution measurement, \geq 1,000 traces were collected to check the electrode surfaces were free from contamination. Analytes were typically studied as solutions (0.1-1 mM) in 1,2,4-trichlorobenzene (TCB; Millipore-Sigma, \geq 99%), tetradecane (TD; Millipore-Sigma, >99%), or propylene carbonate (PC; Millipore-Sigma, anhydrous, \geq 99.7%).

STM-BJ measurements in PC utilized a tip coated in Apiezon wax to minimize background capacitive and Faradaic currents. Voltammetry experiments using a coated gold STM tip as working electrode and gold substrate as counter and reference electrode were performed using a EmStat3+ potentiostat (PalmSens BV, Houten, The Netherlands).

Standard Electrochemical Methods

Standard electrochemical measurements were performed under an argon atmosphere using a CHI760E bipotentiotstat (CH Instruments, Austin, TX, USA) with argon or nitrogen-sparged solutions of 0.1 M tetrabutylammonium hexafluorophosphate ($^n\text{Bu}_4\text{NPF}_6$) in CH_2Cl_2 . Unless otherwise stated, plotted equilibrium voltammograms were obtained at a scan rate of 0.1 V s $^{-1}$ and are not corrected for iR_s . Studies employed glassy carbon disc working electrodes ($\varnothing = 3$ mm, CH Instruments), mechanically polished using an alumina slurry prior to use. Pt wire reference and counter electrodes were cleaned by annealing in an oxyhydrogen flame. Analyte solutions were between 0.1-1 mM. Potentials are reported relative to $[\text{Cp}_2\text{Fe}]^+/\text{[Cp}_2\text{Fe]}$, measured against an internal Cp^*_2Fe reference (-0.532 mV vs $[\text{Cp}_2\text{Fe}]^+/\text{[Cp}_2\text{Fe]}$).

Computational Details

Tunnel Coupling

Density functional theory (DFT) calculations were performed using the Q-Chem 5.4.2 program, using the molecular editor and visualization package IQMol 2.15.1.¹³ Input structures of simplified **Os1**, **Si1**, and **C1** models comprising just two thioether contact groups – **Os1h**, **Si1h**, and **C1h**, respectively – were constructed by addition of those groups to the parent structures determined through single-crystal X-ray diffraction.^{2,14,15} The geometries of these input structures were subsequently separately optimized without gold clusters at the PBE or B3LYP level of theory,

using in each case a 6-31G** basis for light atoms and LACVP for osmium (and for gold, below). Isosurface plots for the frontier orbitals of these isolated molecules calculated using the B3LYP functional are provided in **Figure S17**.

Single gold atoms were next added, linked to the sulfur atoms of these structures, which were then subjected to further geometry optimization with both functionals. The difference in energies between the HOMO and LUMO levels of the molecules bound to the Au₁ clusters (= 2t, a measure of the tunnel coupling^{16,17}) was used to calculate 4t². Isosurface plots for these frontier orbitals, calculated using the B3LYP functional, are provided for the **Os1h** model bound to Au₁ clusters in **Figure S19**.

Geometry optimizations were considered converged when the gradient, and either the energy or atomic displacement, satisfied the convergence criteria (energy = 10×10^{-8} , gradient = 10×10^{-6} , atomic displacement = 1200×10^{-6} ; all values in atomic units [a.u.]). Unless otherwise stated, calculations used the direct inversion in the iterative subspace (DIIS) self-consistent field (SCF) optimization algorithm, using an on-the-fly (automated) superposition of atomic densities (AUTOSAD) initial guess. The SCF cycle was considered converged when the wave function error between consecutive SCF cycles was less than 10^{-8} a.u. When using the PBE functional, the geometries of model compounds bound to Au₁ clusters were optimized using the geometric direct minimization (GDM) self-consistent field optimization algorithm. The SCF cycle was considered converged when the wave function error between consecutive SCF cycles was less than 10^{-4} a.u.

Ab Initio Quantum Transport Calculations Details

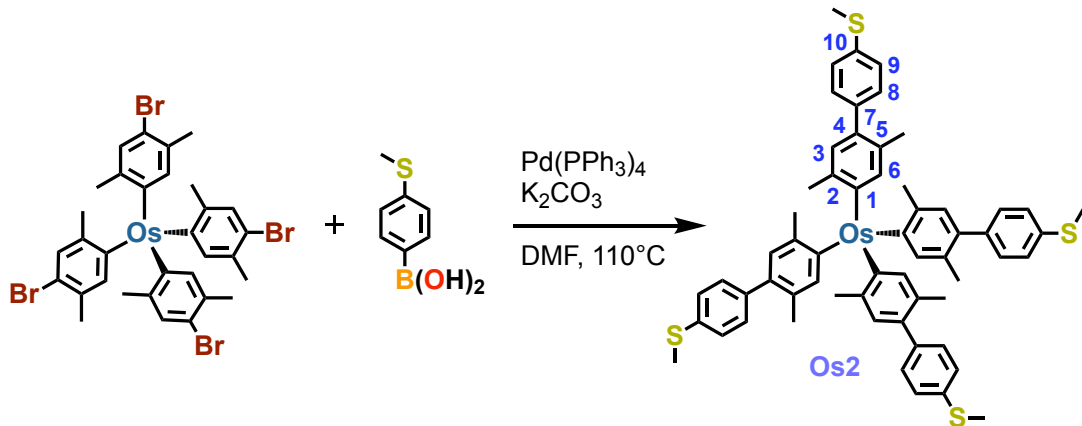
Our ab initio transport calculations were performed using the FHI-aims package,¹⁸ which implements a closed-shell formulation of Kohn-Sham density functional theory. We employed the PBE exchange-correlation functional¹⁹ as a non-empirical, generalized gradient approximation to the exchange-correlation energy. Scalar relativistic effects were included through the zeroth-order regular approximation (ZORA) to account for relativistic corrections to the kinetic energy.²⁰ FHI-aims employs an optimized all-electron numeric atom-centered basis set. For this study, we considered the “light” computational settings, which correspond roughly to double-zeta basis set quality. The ground-state calculations were converged using reliable criteria for the self-consistent field cycle: 10^{-5} electrons/Å³, for the difference in the particle density between consecutive SCF iterations; 10^{-7} eV, for the difference in the total energy; 10^{-4} eV, for the difference of the sum of Kohn-Sham eigenvalues and 10^{-4} eV/Å, for the difference of the forces.

The geometries of the model molecular junctions were determined using a well-established two-step process. First, the positions of the molecular atoms and the apex of the electrodes were optimized using the trust-radius enhanced variant of the Broyden-Fletcher-Goldfarb-Shanno algorithm¹⁸ implemented in FHI-aims. For this optimization, we employ pyramidal gold clusters consisting of up to 11 gold atoms per pyramid. The molecular junction geometries were considered to be structurally relaxed only when all the components of the residual forces per atom were below the threshold value of 10^{-2} eV/Å. Next, the optimized molecular and tip geometries from previous step were held fixed while additional layers of gold atoms were added to the outer planes of the previously optimized electrode tips. This ensures proper screening of excess charge and accurate level alignment for the subsequent quantum transport calculations.

The energy-dependent electronic transmission functions were computed within the linear response regime using the non-equilibrium Green's function formalism, as implemented in the AITRANSS transport module.^{21–23} Each junction electrode was represented by a pyramidal face-centered cluster consisting of 37 atoms, cut from a crystal grown in the (111) direction with closest interatomic distance of 2.88 Å. The electrode self-energies were approximated by an energy-independent (Markovian) local model, given by $\Sigma(\mathbf{r}, \mathbf{r}') = i\eta(\mathbf{r})\delta(\mathbf{r} - \mathbf{r}')$. The local absorption rate, $\eta(\mathbf{r})$, was fine-tuned to ensure that the electronic transmission remained stable under smooth, moderate variations in $\eta(\mathbf{r})$ and was considered to be nonzero only in the subspace corresponding to the outermost layers of the finite cluster.

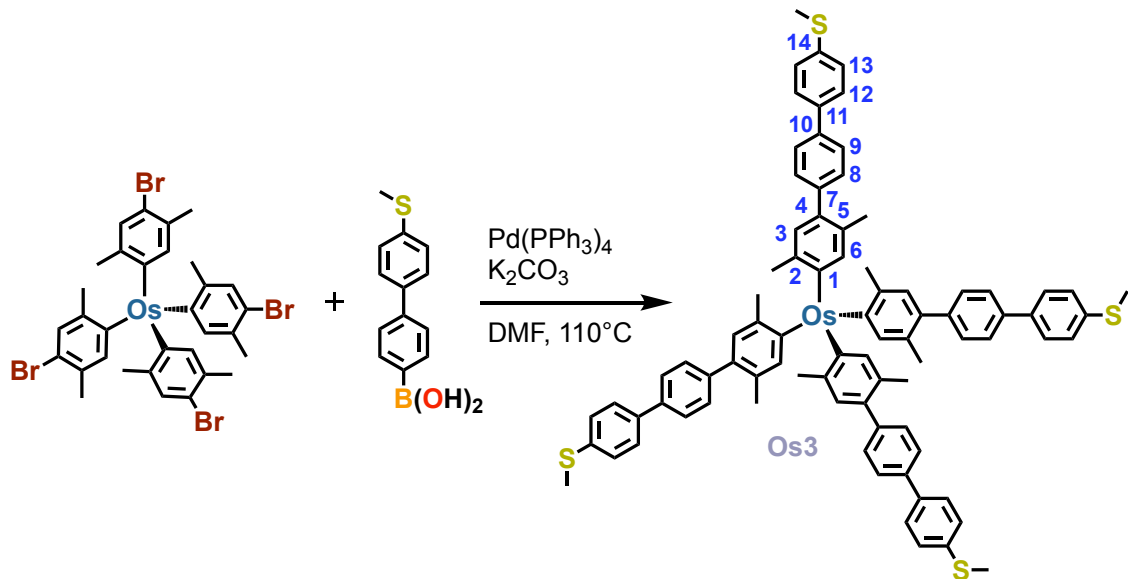
2. Synthetic Details

Tetrakis(2,5-dimethyl-4'-(methylthio)-[1,1'-biphenyl]-4-yl)osmium(IV) (**Os2**)



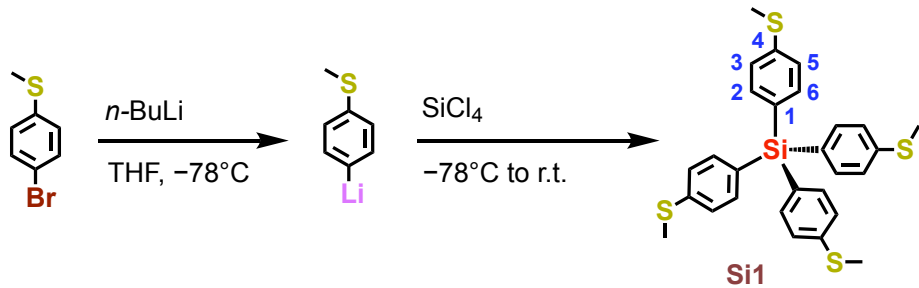
This compound was prepared using an adapted literature method.²⁴ A mixture of tetrakis(4-bromo-2,5-dimethylphenyl)osmium(IV) (0.166 g, 0.179 mmol), 4-(methylthio)phenylboronic acid (0.196 g, 1.17 mmol), $\text{Pd}(\text{PPh}_3)_4$ (0.083 g, 0.072 mmol), and K_2CO_3 (0.143 g, 1.03 mmol) in DMF (5 mL) was heated with stirring to 110°C for 3 d. After cooling to room temperature, solvent was removed under vacuum. The crude product was dissolved in CH_2Cl_2 , pre-absorbed on Celite, then purified by column chromatography on a hexanes-packed SiO_2 column, eluting with 0:1 → 1:1 v/v CH_2Cl_2 -hexanes. $R_f = 0.30$ (SiO_2 , 1:1 v/v CH_2Cl_2 -hexanes). Removal of solvent from selected fractions provided a black solid (0.067 g, 34%). ¹H NMR (CD_2Cl_2 , 400 MHz): δ (ppm) δ 7.31 (s, 16H, aryl C_{8/9}-H), 6.83 (s, 4H, aryl C₆-H), 6.76 (s, 4H, aryl C₃-H), 2.52 (s, 12H, -SCH₃), 2.44 (s, 12H, C₂-CH₃), 2.26 (s, 12H, C₅-CH₃). ¹³C{¹H} NMR (CD_2Cl_2 , 100 MHz): δ (ppm) 141.39 (aryl, C₄-aryl), 138.28 (aryl), 138.12 (aryl), 138.06 (aryl), 137.60 (aryl, C₁₀-SMe), 135.92 (aryl, C₆-H), 131.28 (aryl, C₅-Me), 130.49 (aryl, C_{8/9}-H), 129.28 (aryl, C₃-H), 126.47 (aryl, C_{8/9}-H), 25.62 (C₂-CH₃), 20.55 (C₅-CH₃), 15.99 (-SCH₃). HR-MS (MALDI+) m/z : 1100.3193 ([M]⁺ calc. for $\text{C}_{60}\text{H}_{60}\text{OsS}_4$: 1100.3193).

Tetrakis(2,5-dimethyl-4''-(methylthio)-[1,1':4',1''-terphenyl]-4-yl)osmium(IV) (Os3)



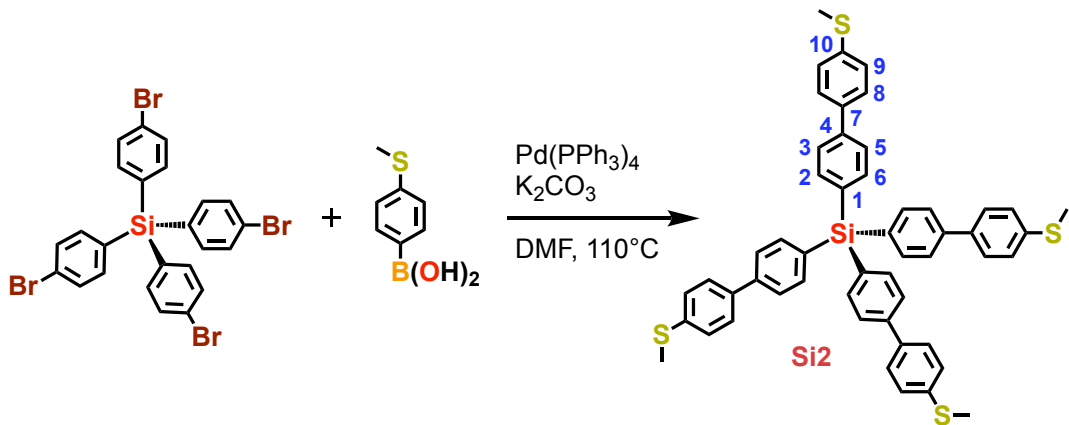
This compound was prepared using an adapted literature method.²⁴ A mixture of tetrakis(4-bromo-2,5-dimethylphenyl)osmium(IV) (0.097 g, 0.105 mmol), 4-(4-methylthiophenyl)phenylboronic acid (0.165 g, 0.676 mmol), Pd(PPh₃)₄ (0.063 g, 0.055 mmol), and K₂CO₃ (0.095 g, 0.687 mmol) in DMF (5 mL) was heated with stirring to 110°C for 3 d. After cooling to room temperature, solvent was removed under vacuum. The crude product was dissolved in CH₂Cl₂, pre-absorbed on Celite, then purified by column chromatography on a hexanes-packed SiO₂ column, eluting with 0:1→1:1 v/v CH₂Cl₂-hexanes. R_f = 0.22 (SiO₂, 1:1 v/v CH₂Cl₂-hexanes). Removal of solvent from selected fractions provided a black solid (0.017 g, 12%) that was subsequently stored at -20°C. ¹H NMR (CDCl₃, 400 MHz): δ (ppm) 7.63 (d, 8H, J = 8.4 Hz, aryl-H), 7.59 (d, 8H, J = 8.4 Hz, aryl-H), 7.46 (d, 8H, J = 8.4 Hz, aryl-H), 7.35 (d, 8H, J = 8.5 Hz, aryl-H), 6.94 (s, 4H, aryl C₆-H), 6.80 (s, 4H, aryl C₃-H), 2.54 (s, 12H, -SCH₃), 2.47 (s, 12H, C₂-CH₃), 2.31 (s, 12H, C₅-CH₃). ¹³C{¹H} NMR (CDCl₃, 101 MHz): δ (ppm) 141.08 (aryl, C₄-aryl), 140.39 (aryl, C₇-aryl), 138.95 (aryl), 138.23 (aryl), 138.03 (aryl), 137.79 (aryl), 137.71 (aryl), 136.57 (aryl, C₆-H), 130.84 (aryl, C₅-Me), 130.35 (aryl C_{8/9}-H), 129.09 (aryl, C₃-H), 127.53 (aryl C-H), 127.12 (aryl C-H), 126.50 (aryl C-H), 25.69 (C₂-CH₃), 20.61 (C₅-CH₃), 16.07 (-SCH₃). HR-MS (MALDI+) m/z: 1404.4428 ([M]⁺ calc. for C₈₄H₇₆OsS₄: 1404.4445).

*Tetrakis(4-(methylthio)phenyl)silane (**Si1**)*



This compound was prepared using adapted literature methods.⁶ 2.5 M *n*-BuLi in hexanes (4.70 mL, 11.8 mmol) was added dropwise at -78°C to a stirred solution of 4-bromothioanisole (2.612 g, 12.86 mmol) in THF (10 mL). After 1 h at -78°C, silicon tetrachloride (0.30 mL, 2.6 mmol) was added to the reaction mixture, which was stirred at -78°C for an additional 1 h then at room temperature for 1 d. Solvent was removed by rotary evaporation, whereby the crude product was dissolved in CH₂Cl₂, pre-absorbed on Celite, then purified by column chromatography on a hexanes-packed SiO₂ column, eluting with 0:1→1:1 v/v CH₂Cl₂-hexanes. R_f = 0.18 (SiO₂, 1:1 v/v CH₂Cl₂-hexanes). Removal of solvent from selected fractions provided a white solid (0.028 g, 2%). ¹H NMR (CD₂Cl₂, 500 MHz): δ (ppm) 7.48 (d, 8H, J = 8.3 Hz, aryl C_{2/6}-H), 7.18 (d, 8H, J = 7.5 Hz, aryl C_{3/5}-H), 2.47 (-SCH₃). ¹³C{¹H} NMR (CD₂Cl₂, 101 MHz): δ (ppm) 142.60 (aryl, C₄-SMe), 134.87 (aryl, C-H), 129.86 (aryl, C₁-Si), 125.40 (aryl, C-H), 15.05 (-SCH₃). HR-MS (EI+) *m/z*: 520.0851 (weak, [M]⁺ calc. for C₂₈H₂₈S₄Si: 520.0843).

*Tetrakis(4'-(methylthio)-[1,1'-biphenyl]-4-yl)silane (**Si2**)*



This compound was prepared using an adapted literature method.²⁴ A mixture of tetrakis(4-bromophenyl)silane (0.109 g, 0.167 mmol), 4-(methylthio)phenylboronic acid (0.158 g, 0.940 mmol), Pd(PPh₃)₄ (0.074 g, 0.064 mmol), and K₂CO₃ (0.137 g, 0.991 mmol) in DMF (5 mL) was

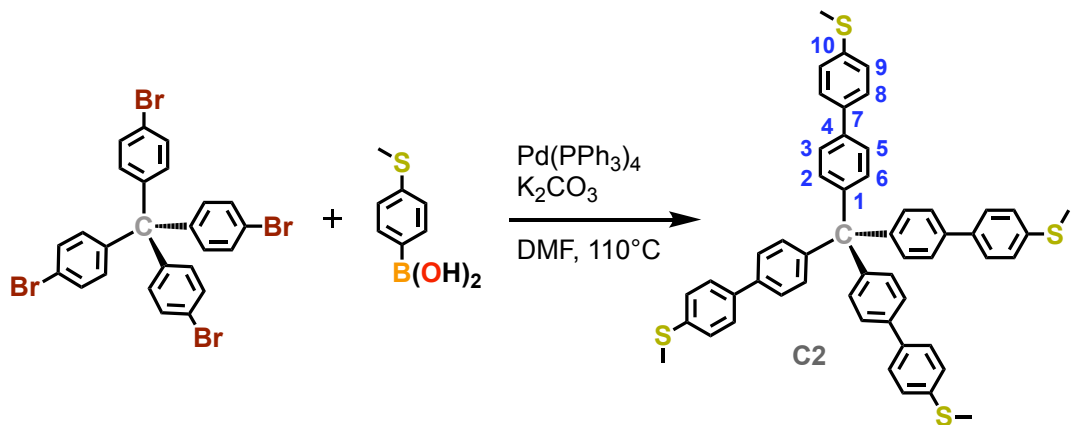
heated with stirring to 110°C for 3 d. After cooling to room temperature, solvent was removed under vacuum. The crude product was dissolved in CH₂Cl₂, pre-absorbed on Celite, then purified by column chromatography on a hexanes-packed SiO₂ column, eluting with 0:1→1:1 v/v CH₂Cl₂-hexanes. R_f = 0.27 (SiO₂, 1:1 v/v CH₂Cl₂-hexanes). Removal of solvent from selected fractions provided a white solid (0.041 g, 30%). ¹H NMR (CD₂Cl₂, 400 MHz): δ (ppm) 7.72 (d, 8H, J = 8.3 Hz, aryl-H), 7.66 (d, 8H, J = 8.5 Hz, aryl-H), 7.59 (d, 8H, J = 8.7 Hz, aryl-H), 7.34 (d, 8H, J = 8.7 Hz, aryl-H), 2.52 (-SCH₃). ¹³C{¹H} NMR (CD₂Cl₂, 101 MHz): δ (ppm) 142.05 (aryl, C-R), 138.78 (aryl, C₁₀-SMe), 137.64 (aryl, C-R), 137.28 (aryl, C-H), 133.18 (aryl, C-R), 127.79 (aryl, C-H), 127.03 (aryl, C-H), 126.64 (aryl, C-H), 15.84 (-SCH₃). HR-MS (MALDI+) *m/z*: 824.2084 ([M]⁺ calc. for C₅₂H₄₄S₄Si: 824.2095).

Tetrakis(4-(methylthio)phenyl)methane (C1)



This compound was prepared using an adapted literature method.²⁵ A solution of tetrakis(4-bromophenyl)methane (0.201 g, 0.316 mmol) in DMF (2 mL) was added to solution of sodium thiomethoxide (0.135 g, 1.93 mmol) in DMF (2 mL). The resulting mixture was heated to 65°C and stirred for 1 d. After cooling, solvent was removed under vacuum. The crude product was dissolved in CH₂Cl₂, pre-absorbed on Celite, then purified by column chromatography on a hexanes-packed SiO₂ column, eluting with 0:1→1:1 v/v CH₂Cl₂-hexanes. R_f = 0.30 (SiO₂, 1:1 v/v CH₂Cl₂-hexanes). Removal of solvent from selected fractions provided a white solid (0.027 g, 17%). ¹H NMR (CD₂Cl₂, 400 MHz): δ (ppm) 7.12 (s, 16H, aryl-H), 2.45 (s, 12H, -SCH₃). ¹³C{¹H} NMR (CD₂Cl₂, 101 MHz): δ (ppm) 143.72 (aryl, C₁-C(sp³)), 136.68 (aryl, C₄-SMe), 131.59 (aryl, C-H), 125.73 (aryl, C-H), 15.66 (-SCH₃). HR-MS (ESI+) *m/z*: 504.1066 ([M]⁺ calc. for C₂₉H₂₈S₄: 504.1074).

Tetrakis(4'-(methylthio)-[1,1'-biphenyl]-4-yl)methane (C2)



This compound was prepared using an adapted literature method.²⁴ A mixture of tetrakis(4-bromophenyl)methane (0.111 g, 0.175 mmol), 4-(methylthio)phenylboronic acid (0.180 g, 1.07 mmol), $\text{Pd}(\text{PPh}_3)_4$ (0.073 g, 0.063 mmol), and K_2CO_3 (0.131 g, 0.948 mmol) in DMF (5 mL) was heated with stirring to 110°C for 3 d. After cooling to room temperature, solvent was removed under vacuum. The crude product was dissolved in CH_2Cl_2 , pre-absorbed on Celite, then purified by column chromatography on a hexanes-packed SiO_2 column, eluting with 0:1→1:1 v/v CH_2Cl_2 -hexanes. $R_f = 0.25$ (SiO_2 , 1:1 v/v CH_2Cl_2 -hexanes). Removal of solvent from selected fractions provided a white solid (0.013 g, 9%). ^1H NMR (CDCl_3 , 500 MHz): δ (ppm) 7.53 (m, 16H, aryl- H), 7.38 (d, 4H, $J = 8.5$ Hz, aryl- H), 7.31 (d, 4H, $J = 8.5$ Hz, aryl- H), 2.52 (s, 12H, - SCH_3). $^{13}\text{C}\{\text{H}\}$ NMR (CDCl_3 , 126 MHz): δ (ppm) 145.84 (aryl, CR_3), 138.14 (aryl, CR_3), 137.71 (aryl, CR_3), 137.48 (aryl, CR_3), 131.67 (aryl, C-H), 127.43 (aryl, C-H), 127.06 (aryl, C-H), 126.06 (aryl, C-H), 16.02 (- SCH_3). HR-MS (EI+) m/z : 808.2321 ([M]⁺ calc. for $\text{C}_{53}\text{H}_{44}\text{S}_4$: 808.2326).

3. Electrochemistry

Table S1. Electrochemical data for selected Os(aryl)₄ complexes.^a

	redox transition	$E_{1/2}$ (V)	E_{pa} (V)	E_{pc} (V)	ΔE (V)	i_{pa}/i_{pc}	ref.
Os(C₈H₈-SMe)₄ (Os1)	1-/0	-1.955	-1.920	-1.990	0.070	0.94	5
	0/1+	+0.018	+0.056	-0.020	0.076	0.99	
	1+/2+	+0.650	+0.700	+0.600	0.100	0.98	
Os(C₈H₈-C₆H₄-SMe)₄ (Os2)	1-/0	-1.906	-1.868	-1.944	0.076	1.05	this work
	0/1+	+0.228	+0.271	+0.186	0.085	1.02	
	1+/2+	-	-	-	-	-	
Os(C₈H₈-C₆H₄-C₆H₄-SMe)₄ (Os3)	1-/0	-1.927	-1.861	-1.994	0.133	1.02	this work
	0/1+	+0.222	+0.273	+0.172	0.101	1.02	
	1+/2+	-	-	-	-	-	
Os(C₈H₉)₄	1-/0	-2.008	-1.969	-2.047	0.078	0.98	2
	0/1+	+0.244	+0.281	+0.208	0.073	1.00	
	1+/2+	-	-	-	-	-	
Os(C₈H₈-C₆H₄-C₆H₅)₄	1-/0	-	-	-	-	-	26
	0/1+	+0.21	-	-	-	-	
	1+/2+	+1.05	-	-	-	-	

^a Scan rate = 0.1 V s⁻¹; Supporting electrolyte = ⁿBu₄NPF₆-CH₂Cl₂; working electrode: glassy carbon; reference electrode, counter electrode: Pt. All potentials are reported relative to [Cp₂Fe]⁺/Cp₂Fe, corrected for iR_s .

4. UV-Vis Spectroscopy

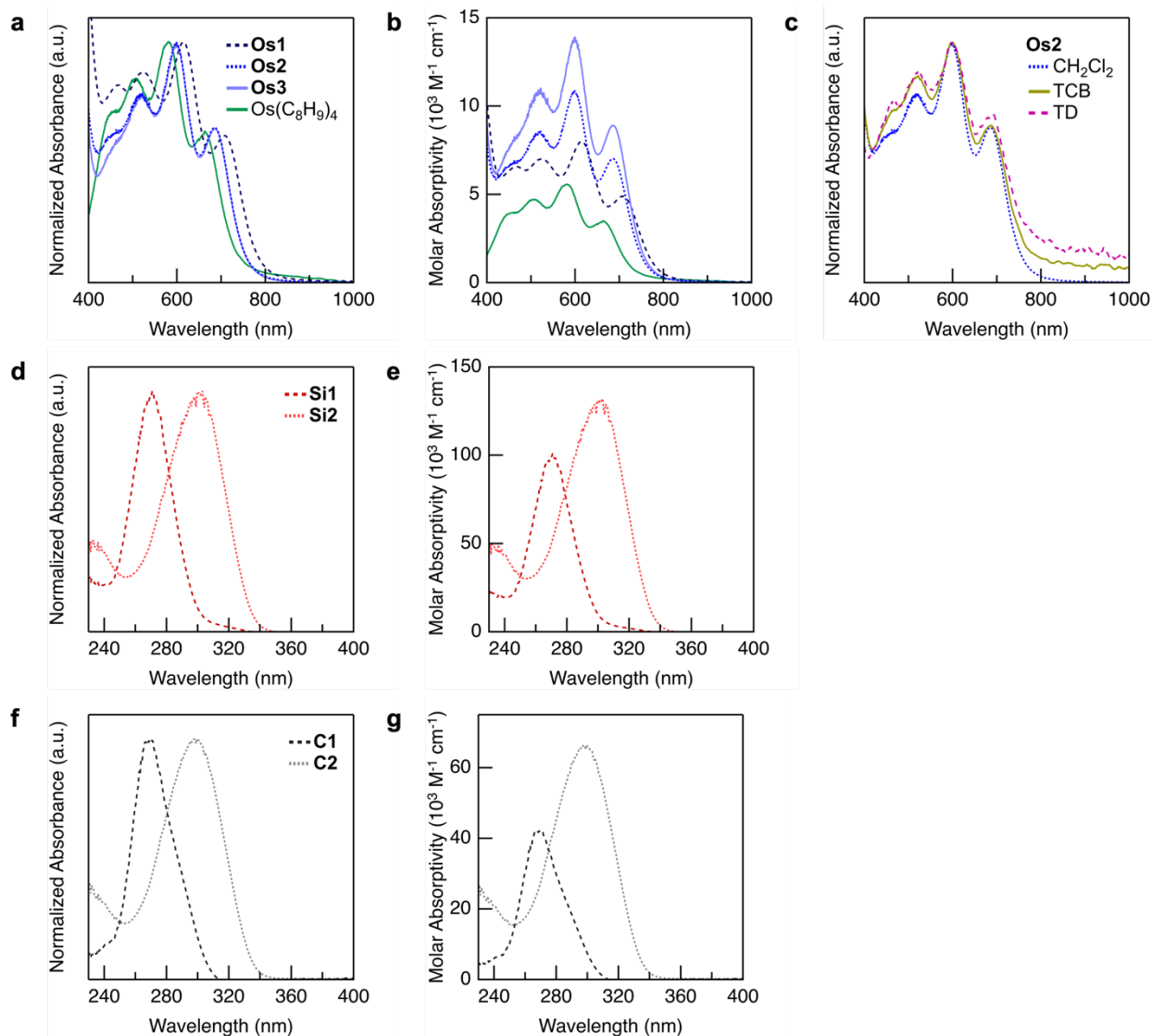


Figure S1. **(a-b)** Overlaid UV-vis spectra for **Os1**,⁵ **Os2**, **Os3**, and **Os(xylyl)₄**⁵ (all spectra measured using a 10 mm pathlength cell in **CH₂Cl₂**, unless stated). In (a), absorbance spectra are normalized to the peak of maximum intensity in the visible region. Data for **Os1-3** are reproduced from **Figure 2c** for convenience. In (b), plots of molar absorptivity against wavelength reveal the extended complexes are more efficient at absorbing visible light. **(c)** Overlaid normalized spectra for **Os2** measured in **TCB**, **TD** (1 mm pathlength cell), and **CH₂Cl₂** (reproduced from panel (a) and **Figure 2c**). These studies reveal no significant changes to the wavelengths of primary absorption maxima that might indicate bulk protonation/oxidation in the chlorinated solvents. **(d-e)** Plots analogous to those in panels (a) and (b) for **Si1** and **Si2**. **(f-g)** Plots analogous to those in panels (a) and (b) for **C1** and **C2**. Data extracted from these measurements are provided in **Table S2**.

Table S2. Spectroscopic and frontier orbital energy gap data for selected compounds.^a

	λ_{\max} (nm)	ϵ_{\max} (M ⁻¹ cm ⁻¹)	E_{opt} (nm) ^b	$E_{\text{elec}} (\text{V})^c$	ref./comments
Os(C ₈ H ₈ -SMe) ₄ (Os1)	465 525 613 705	6,568 7,004 7,951 4,888	784	1.973	⁵
Os(C ₈ H ₈ -C ₆ H ₄ -SMe) ₄ (Os2)	462 516 598 685	6,707 8,560 10,872 7,020	758	2.134	this work
Os(C ₈ H ₈ -C ₆ H ₄ -SMe) ₄ (Os2) [in TCB]	464 519 598 687	5,521 6,628 7,740 5,056	-	-	this work
Os(C ₈ H ₈ -C ₆ H ₄ -SMe) ₄ (Os2) [in TD]	466 522 600 689	2,622 3,052 3,466 2,414	-	-	this work
Os(C ₈ H ₈ -C ₆ H ₄ -C ₆ H ₄ -SMe) ₄ (Os3)	452sh 519 598 685	7,838 10,890 13,889 8,902	757	2.149	this work
Os(C ₈ H ₉) ₄	454 503 580 662	3,857 4,710 5,570 3,513	744	2.252	[2], this work
Si(C ₆ H ₄ -SMe) ₄ (Si1)	271	100,970 ^d	300	-	this work
Si(C ₆ H ₄ -C ₆ H ₄ -SMe) ₄ (Si2)	303	132,090 ^d	335	-	this work
C(C ₆ H ₄ -SMe) ₄ (C1)	270	42,277 ^d	304	-	this work
C(C ₆ H ₄ -C ₆ H ₄ -SMe) ₄ (C2)	299	66,442 ^d	333	-	this work

^a Measured in CH₂Cl₂ unless otherwise stated. ^b Defined here as the longest wavelength at which absorbance reaches ~10% of the peak of maximum intensity in the visible region. ^c Calculated from solution electrochemical studies: $E_{\text{elec}} = E_{1/2}(0/1+) - E_{1/2}(1-/0)$. ^d High ϵ_{\max} have been reported for other tetra(oligoaryl)silane and methane complexes. For example, 51,000 M⁻¹ cm⁻¹ for tetrakis(4-(thiophen-2-yl)phenyl)methane,²⁷ and up to 1.9×10⁶ M⁻¹ cm⁻¹ for a tetrakis(tetraaryl)silane with ligand arms comprising fluorene groups.²⁸

5. Additional Conductance Data

Table S3. Conductance values for selected compounds.^a

compound/ peak (assigned geometry)	conductance (G_0)			
	TD		TCB	
	low G (intact molecule)	high G (ligand arm)	low G (intact molecule)	high G (ligand arm)
Os1 ^b	3.7×10^{-5}	6.5×10^{-3}	-	-
Si1 ^b	3.5×10^{-5}	6.6×10^{-3}	-	-
C1 ^b	2.0×10^{-5}	- ^c	-	-
Os2	1.9×10^{-6}	8.4×10^{-4}	- ^d	1.2×10^{-4}
Os2 (2)	3.2×10^{-6}	7.1×10^{-4}	-	-
Si2	3.5×10^{-7}	9.5×10^{-4}	4.3×10^{-7}	9.7×10^{-4}
Si2 (2)	-	-	3.7×10^{-7}	7.2×10^{-4}
C2	- ^c	7.6×10^{-4}	6.0×10^{-7}	8.6×10^{-4}
C2 (2)	-	-	6.9×10^{-7}	1.5×10^{-4}
Os3	$\sim 2.5 \times 10^{-7}$	1.2×10^{-4}	- ^d	1.5×10^{-4}

^a All values from measurements at $V_{\text{bias}} = 750$ mV from peak fits to histograms (1), unless otherwise stated. Blue shaded entries correspond to repeated measurements. ^b $V_{\text{bias}} = 250$ mV. ^c Peak not observed in conductance histograms. ^d Value not reported due to the large apparent conductance variability for this junction geometry when measured in this solvent.

Reproducibility Studies in TD

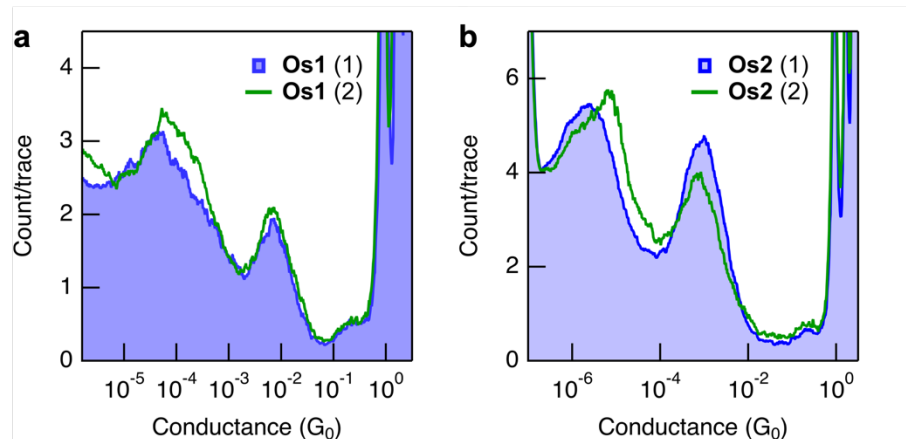


Figure S2. Overlaid 1D histograms for repeated conductance measurements of (a) **Os1** ($V_{\text{bias}} = 250$ mV) and (b) **Os2** ($V_{\text{bias}} = 750$ mV) in TD. This data suggests there is a greater consistency between measurements obtained using TD than TCB for these Os(aryl)₄ complexes (see **Figure S5**).

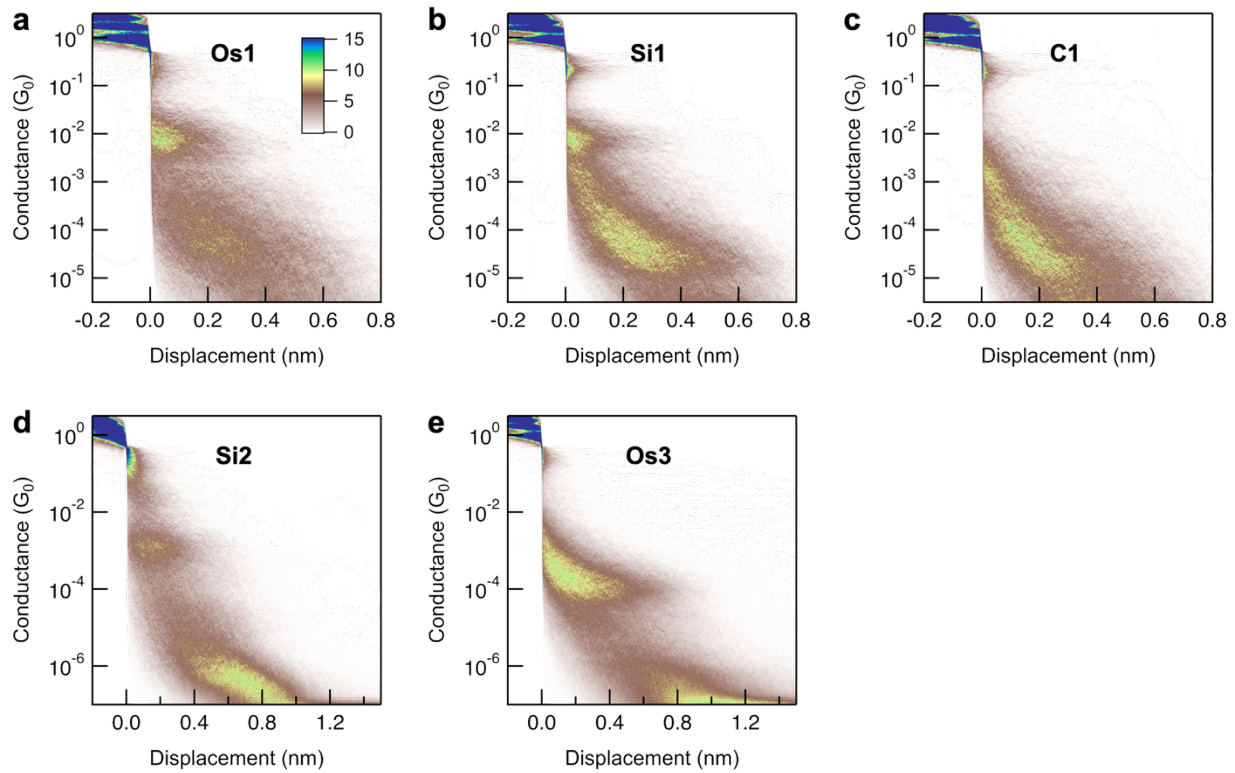


Figure S3. 2D histograms for (a) Os1, (b) Si1, (c) C1 ($V_{bias} = 250$ mV), (d) Si2, and (e) Os3 ($V_{bias} = 750$ mV), corresponding to the 1D histograms shown in **Figure 3**.

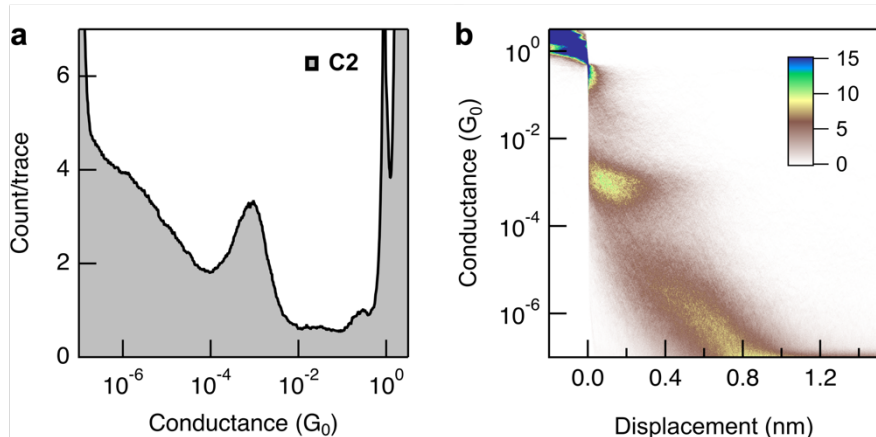


Figure S4. (a) 1D and (b) 2D histogram obtained for measurements of a solution of C2 in TD ($V_{bias} = 750$ mV). The low conductance feature is absent/poorly resolved.

Reproducibility Studies in TCB

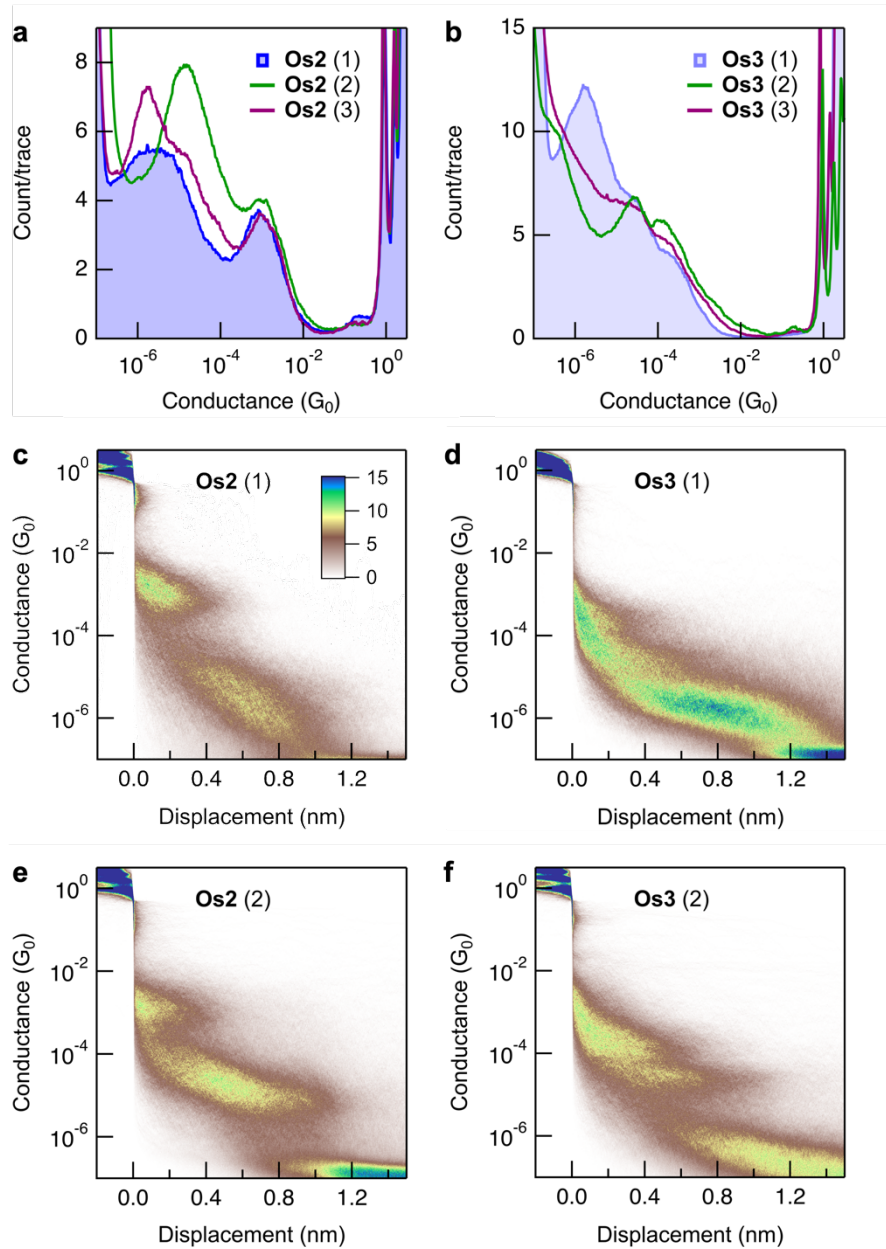


Figure S5. Overlaid 1D histograms for repeated conductance measurements of (a) **Os2** and (b) **Os3** in TCB at $V_{bias} = 750$ mV. (c-f) Example 2D histograms corresponding to selected 1D histograms in (a,b). This data shows that the low conductance features attributed to junctions comprising the intact complexes exhibit a large experiment to experiment variability when measured in TCB. The low conductance step observed for **Os3** extends to ~ 1.4 nm displacement. While this is shorter than the S-S distance of 2.6 nm calculated for this compound, it is close to the junction displacement expected if the difference in step length between **Os1** and **Os2** (~ 0.6 nm) is added to the displacement of **Os2** (~ 1 nm).

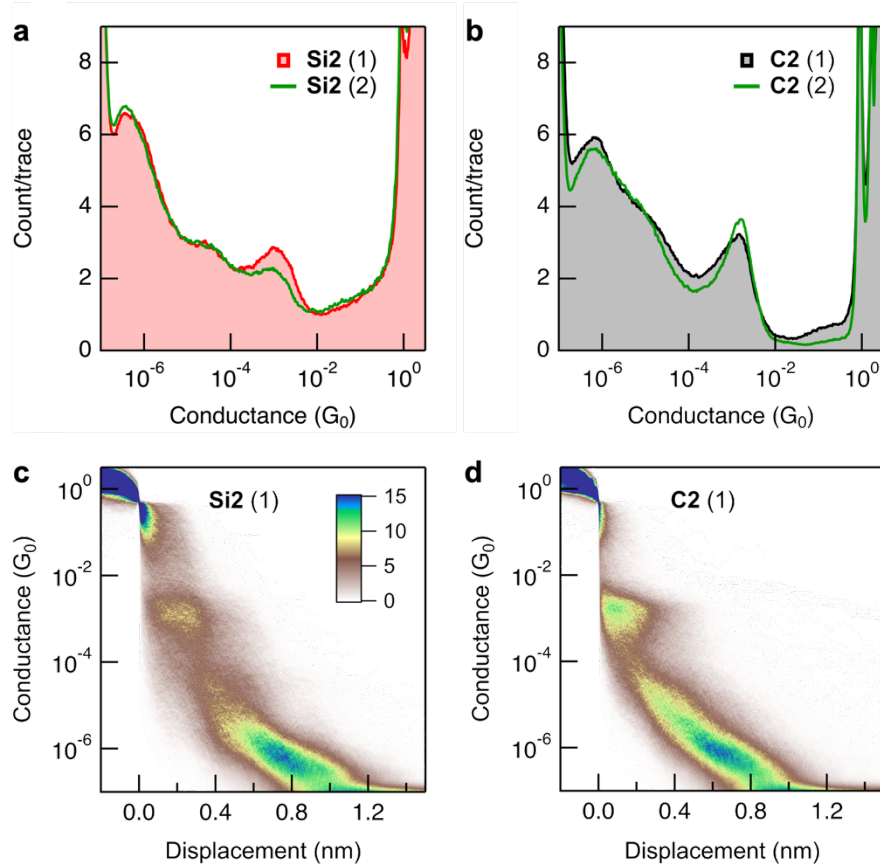


Figure S6. Overlaid 1D histograms for repeated conductance measurements of (a) Si2 and (b) C2 in TCB at $V_{\text{bias}} = 750$ mV. (c-d) Example 2D histograms corresponding to selected 1D histograms in panels (a) and (b). This data shows that the low conductance features attributed to junctions comprising the intact compounds exhibit a better reproducibility when measured in TCB than the Os(aryl)₄ complexes.

Analysis of High Conductance Features

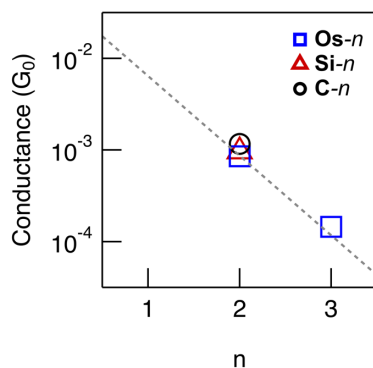


Figure S7. A plot of conductance versus number of aryl groups in each ligand for the high conductance peak feature observed in each series of wires **Os-*n***, **Si-*n***, **C-*n***, measured in TCB. Grey dashed line is the fit of conductance versus *n* for **Os-*n*** measured in TD (Figure 3e), included here for comparison.

The junction geometries of the high conductance features observed in measurements of **Os-*n***, **Si-*n***, and **C-*n*** (Figure 3a-c) cannot yet be comprehensively assigned. Additional experiments and analysis relevant to this question are presented below.

To evaluate the possibility that these features correspond to cleaved linker arms, in Figure S8 we overlay histograms obtained for conductance measurements of **Os2**, **Si2**, and **C2** with that of (4'-(methylthio)-[1,1'-biphenyl]-4-yl)(triphenylphosphine)gold(I) (**Au2**) in TCB. This complex comprises the same biphenyl ligand as found in the tetrahedral compounds but now coordinated directly to a gold(I) center. This, as well as a series of analogous compounds, has previously been used to substantiate the formation of chemisorbed Au–C(sp^2) contacts from precursors comprising $-\text{SnMe}_3$,²⁹ $-\text{B}(\text{OH})_2$,³⁰ or $-\text{I}$ groups.⁷ Interestingly, we find that the conductance of junctions formed from **Au2** are close to (albeit a factor of 2-3 higher than) those of the high conductance peaks formed through the proposed ligand dissociation reaction (Figure S10), substantiating but not fully justifying this explanation. If these peak features do correspond to junctions formed from the same species, we hypothesize that their distinct conductance values must result from changes in the chemical environment near the junction (e.g., significant differences in solution/surface concentration of absorbing species or the presence/absence of coordinating phosphine). Measurements of junctions formed from the same molecular component in different solvents have been reported to exhibit different conductance values, where the energetic alignment between the

dominant conducting orbital and E_F , or the most probably electrode binding geometry, is modified.^{9,31,32}

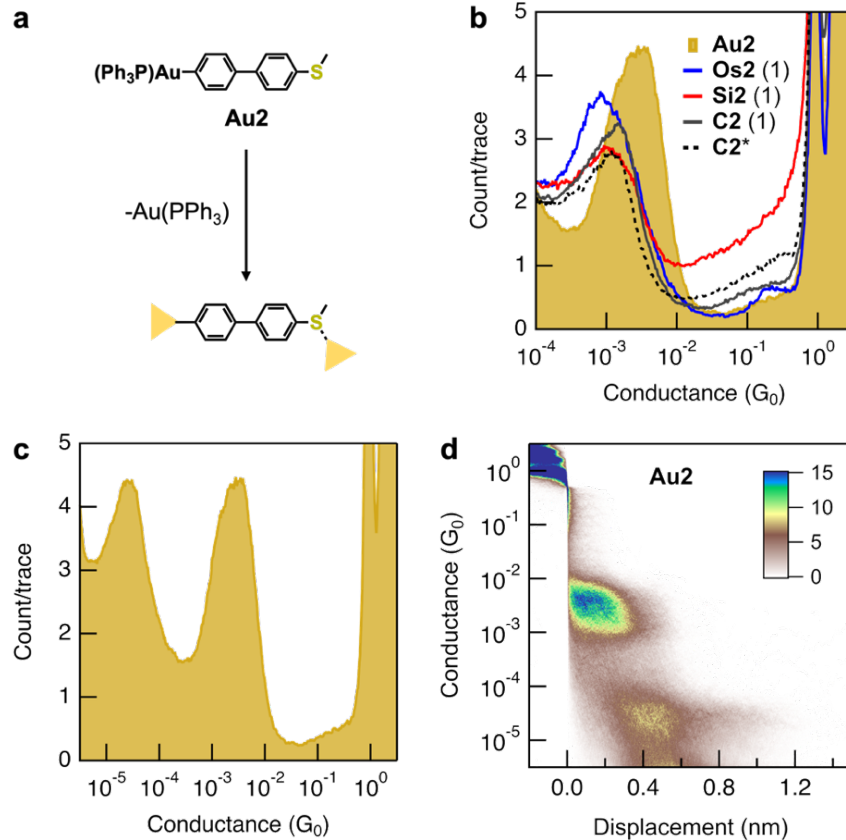


Figure S8. (a) Schematic showing junction formation from **Au2**, a complex containing a preinstalled Au–C bond. (b) Overlaid 1D histograms obtained from measurements of **Os2**, **Si2**, and **C2** (solid lines, $V_{\text{bias}} = 750$ mV), now focused on the high conductance peak around $10^{-3} G_0$, and **Au2** (filled, $V_{\text{bias}} = 100$ mV) in TCB (6,000-10,000 traces). An overlaid histogram of **C2** obtained at $V_{\text{bias}} = 100$ mV (**C2***, dashed, 10,000 traces) indicates the conductance of this peak does not exhibit a large bias dependence. The features for **Os2**, **Si2**, and **C2** are systematically lower in conductance (8.3 to $12.2 \times 10^{-4} G_0$) by a factor of 2-3 compared to the peak seen for **Au2** ($25.3 \times 10^{-4} G_0$). (c) 1D and (d) 2D conductance histograms for **Au2**, plotted to a lower conductance range. The feature at $2.4 \times 10^{-5} G_0$ is attributed to junctions comprising the tetraphenylene dimer formed from the $\text{C}(sp^2)-\text{C}(sp^2)$ homocoupling of two surface adsorbed $\text{MeS-C}_6\text{H}_4-\text{C}_6\text{H}_4-\text{Au}$ species.

Further compounding this discussion, we find that these peak features for **Au2** and **Os2** measured in PC also exhibit conductance differences, now with the feature observed in studies of **Os2** occurring at a higher value (**Figure S14b**). However, we note that the peak features for each

compound also exhibit notable similarities: (i) they do not vary in conductance with changing tip bias; and (ii) their peak intensity is reduced at positive tip biases (**Figure 4a,b** and **S14a**).

Another characteristic feature of the conductance histograms formed from **Au2** is the secondary peak observed at $\sim 2 \times 10^{-5} G_0$, attributable to junctions formed from $\text{MeS-(C}_6\text{H}_4)_4\text{-SMe}$. The unambiguous observation of such a dimer feature in measurements of the tetraaryl systems provide support to the proposal that the high conductance peaks observed correspond to junctions formed from cleaved ligand arms. While no such feature can yet be clearly identified in measurements of **Os-n**, **Si-n**, or **C-n** in TD, TCB, or PC, it is also plausible that these are of low intensity and are obfuscated by the low conductance peak. We recognize that the observation of intense features attributable to dimer junctions requires a high surface concentration of the chemisorbed $\text{Au-C}(sp^2)$ species. Two of these adsorbates must meet to undergo the requisite $\text{C}(sp^2)\text{-C}(sp^2)$ homocoupling reaction. Unlike reactions that form chemisorbed products, the concentration of dimer formed at the surface will not be expected to increase over time as these weakly bound reaction products can readily diffuse away into the bulk solution. Accordingly, there will be a low probability of forming dimer junctions (resulting in a low intensity conductance peak) where the rate of transmetallation from the solution species is relatively slow. Such a possibility is well-illustrated in previous studies of 4-thioanisole boronic acid.^{9,30} Features corresponding to chemisorbed $\text{Au-C}_6\text{H}_4\text{-S(Me)-Au}$ junctions are clearly seen at room temperature whereas well-resolved peak features for the $\text{MeS-(C}_6\text{H}_4)_2\text{-SMe}$ dimer are only observed at elevated temperatures. We cannot rule out this possibility for the tetraaryl compounds studied here. While high performance liquid chromatography experiments³³ have not yet been applied to probe these proposed *in situ* reactions, the anticipated low quantities of reacted materials suggest the robust detection of products could prove challenging.

For completeness, in **Figure S9**, we present representative conductance-displacement traces for **Os2**. These show that individual traces can exhibit high or low conductance features, or both features in the same measurement (most probable). We note that such junction formation statistics are consistent with both geometries proposed for the high conductance peak. Aryl- π contacted junctions may or may not always form, and then they could break to form junctions of the intact molecule or a tunneling gap. Linkers arms may cleave at or proximal to the junction,³⁴ chemisorb to the gold surface, and become trapped in junctions intermittently along with the intact tetraaryl compounds which can self-assemble from solution.

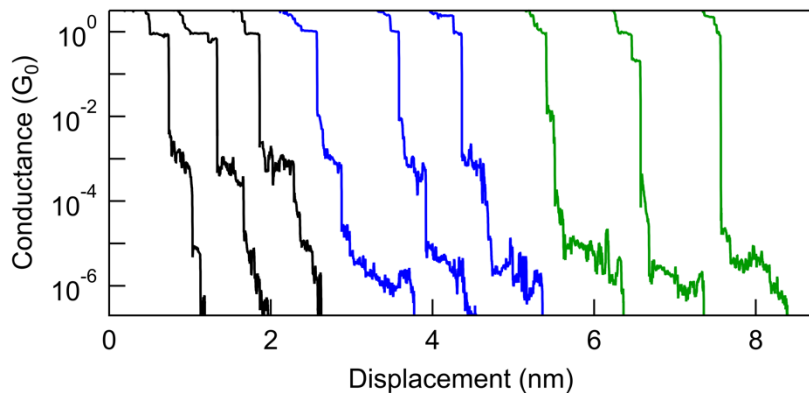


Figure S9. Representative conductance-displacement traces for **Os2** measured in TD showing: *left* (black), high conductance features without significant low conductance plateaus (11% of traces); *middle* (blue) high and low conductance features (56%); and *right* (green) low conductance features only (22%). Traces are offset along the displacement axis for clarity. This data corresponds to the measurement of **Os2** shown in **Figure 3**. The percentages of each type of trace observed were estimated by visual inspection of a representative sample of measurements (1,000 traces).

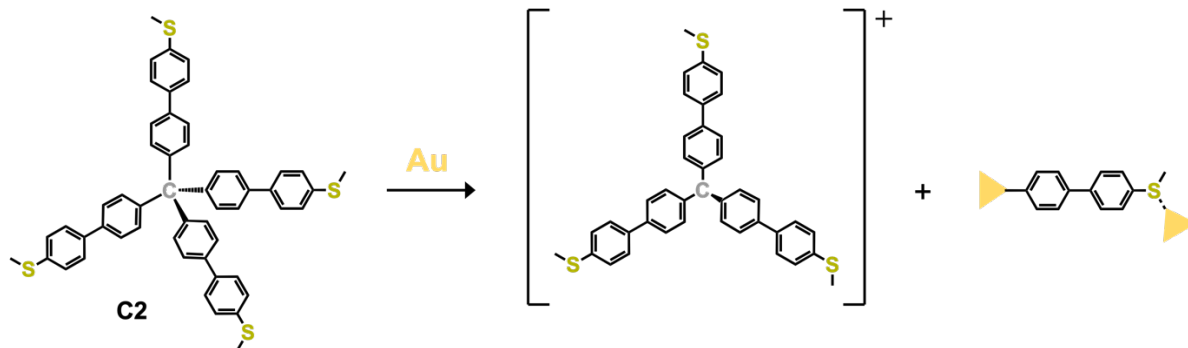


Figure S10. A possible reaction scheme leading to ligand dissociation, using **C2** as a representative example. It is apparent that the thioether-functionalized carbocations so-formed *in situ* from **Os-n**, **Si-n**, and **C-n** could, in principle, also be captured and studied in junctions. Related species were probed in recent single-molecule conductance studies by Prindle *et al.*³⁵ However, as these non-chemisorbed reaction products are free to diffuse away into the bulk, we do not expect them to sufficiently concentrate near the junction to provide high junction formation probabilities in conductance measurements. While the exact mechanism of the proposed C(sp^2)-central atom bond cleavage is unknown, we note that formation of an Au–C(sp^2) bond through direct interaction between a gold surface atom and the C(sp^2) atom of the intact complex(es) appears unfeasible due to steric hinderance. Importantly however, the stability of these tetraaryl compounds in solution – as illustrated by UV-vis (**Figure S1**) and NMR (**Figure S24-S35**) experiments – indicates that if any bond cleavage does occur it must take place near the surface.

Additional Measurements in Propylene Carbonate

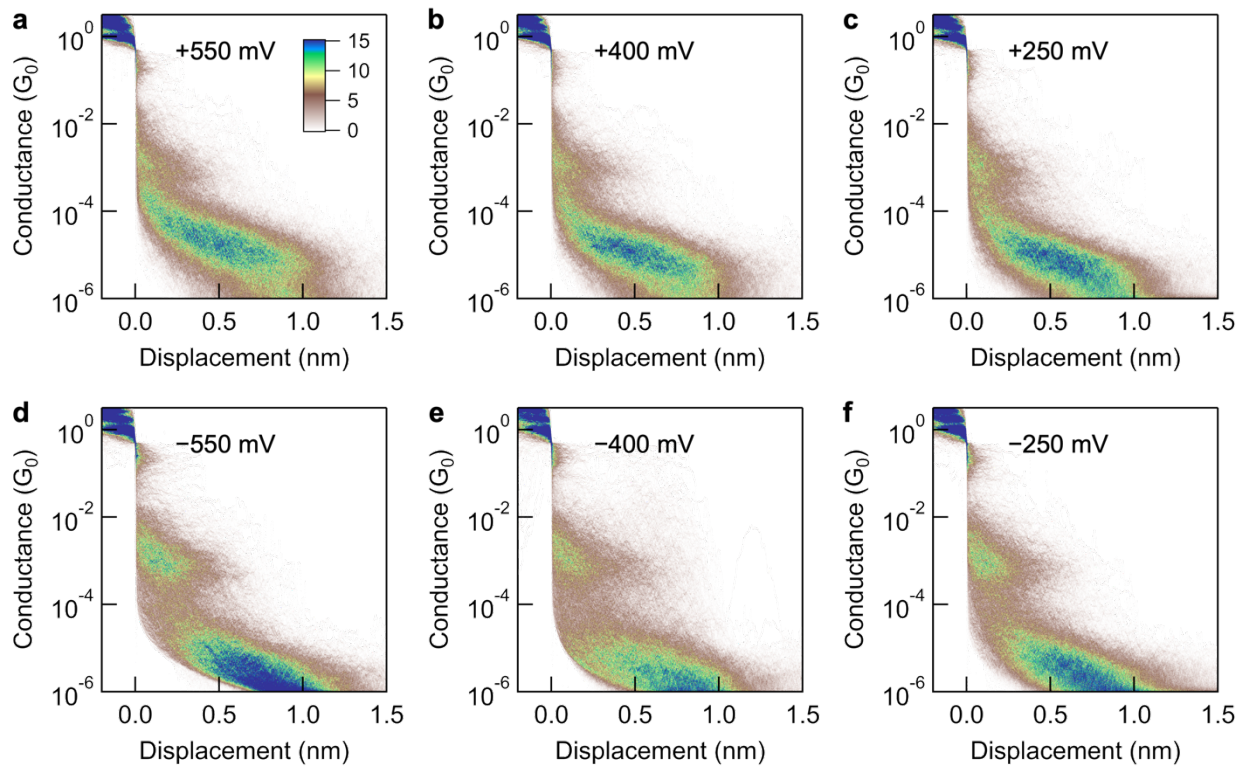


Figure S11. 2D histograms corresponding to the 1D histograms shown in **Figure 4a**.

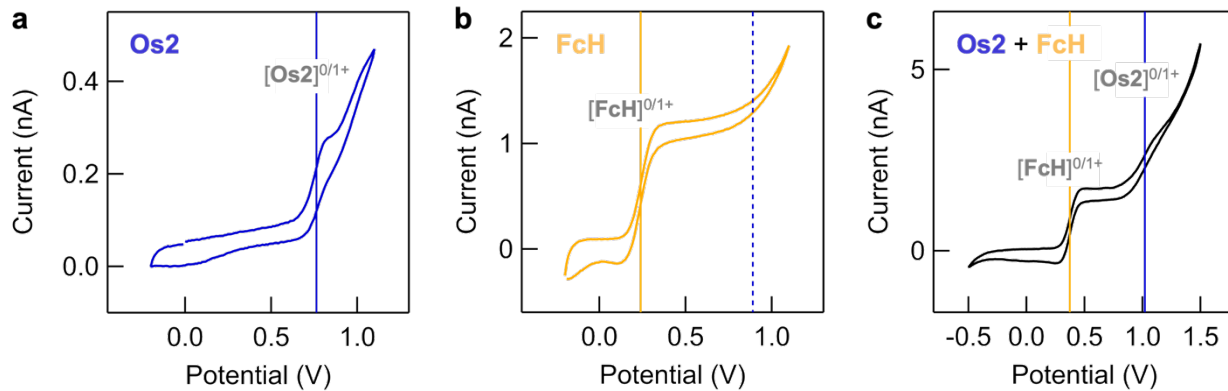


Figure S12. Cyclic voltammograms obtained in PC with no added electrolyte for ~0.5 mM solutions of (a) **Os2** (reproduced from Figure 4f for convenience), (b) ferrocene (**FcH**), and (c) a mixture of **Os2** and **FcH** in a 1:1 molar ratio. Solid vertical lines denote the approximate equilibrium potentials ($E_{1/2}$) for observed redox features.³⁶ The feature observed near the oxidative solvent limit in solutions containing **Os2** is assigned as the 0/1+ couple characteristic of this complex, at approximately +0.65 V vs. $[\text{FcH}]^{0/1+}$ under these conditions. This assignment is corroborated by the absence of this feature in panel (b) (dashed line indicates $E_{1/2}$ vs. $[\text{FcH}]^{0/1+}$ for **Os2**), confirming this is not attributable to an adventitious electroactive contaminant. Voltammograms were obtained with a wax-coated gold STM tip as working ultramicroelectrode, and a gold-on-steel substrate as counter and reference electrode, using an external potentiostat. Redox features at comparable potentials (within the error associated with reference electrode potential drift) were obtained when sweeping the tip-substrate bias and monitoring the tip current using the STM-BJ electronics. The variation in measured currents across these voltammograms is attributed in part to the use of different STM tips which have different electrode areas.

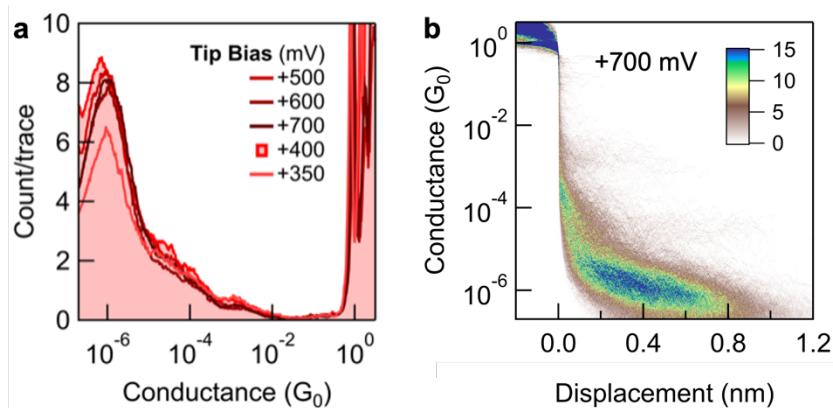


Figure S13. (a) Overlaid 1D histograms for **Si2** measured in propylene carbonate at different V_{bias} (2,000 traces; biases listed in order of measurement). Much smaller conductance changes are observed compared to analogous measurements for **Os2** (Figure 4c). No significant high conductance feature is observed. (b) A representative 2D histogram corresponding to the 1D histogram in panel (a) obtained at tip bias = +700 mV.

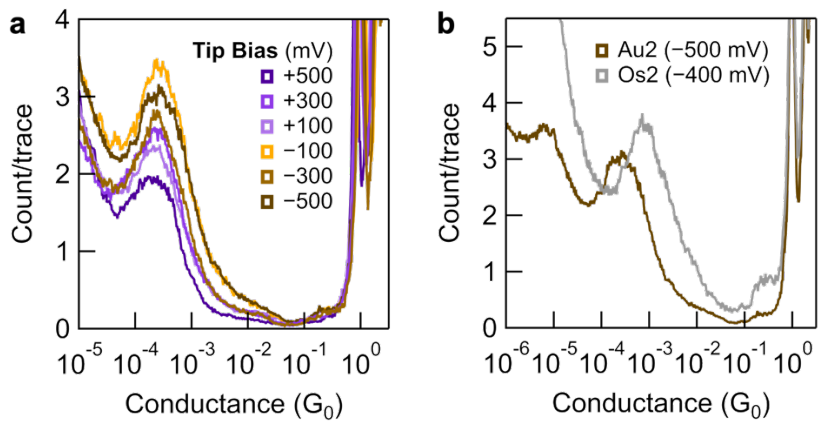


Figure S14. (a) Overlaid 1D histograms for **Au2** measured in PC at different tip biases. The peak feature is assigned to gold-biphenyl-S(Me)-gold junction geometries (**Figure S8a**). While the conductance of this feature does not with tip bias, its intensity is consistently lower when measured at positive, compared to measurements at negative, tip biases. (b) Overlaid 1D histograms for **Au2** and **Os2** measured in PC at comparable negative tip biases, focused on the high conductance peak region. In contrast to the measurements in TD, here this feature for **Os2** is *higher* in conductance ($7.2 \times 10^{-4} G_0$) by a factor of ~ 3 relative to the peak observed for **Au2** ($2.4 \times 10^{-4} G_0$). Data for **Os2** is reproduced here from **Figure 4a** for convenience.

6. Additional Computational Data

Geometric Analysis

We note that the aryl groups of oligoaryl wires with tetrahedral osmium(IV), silane, or methane centers exhibit different geometric relationships to one another in the frozen geometries observed in molecular structures obtained from single-crystal X-ray crystallography or computational experiments. The relationship between two aryl substituents can be defined using two dihedral angles (which we label α and β), as shown in **Figure S15**. Note that the specific α or β labels have no associated special meaning and are interchangeable within a given dihedral angle pair.

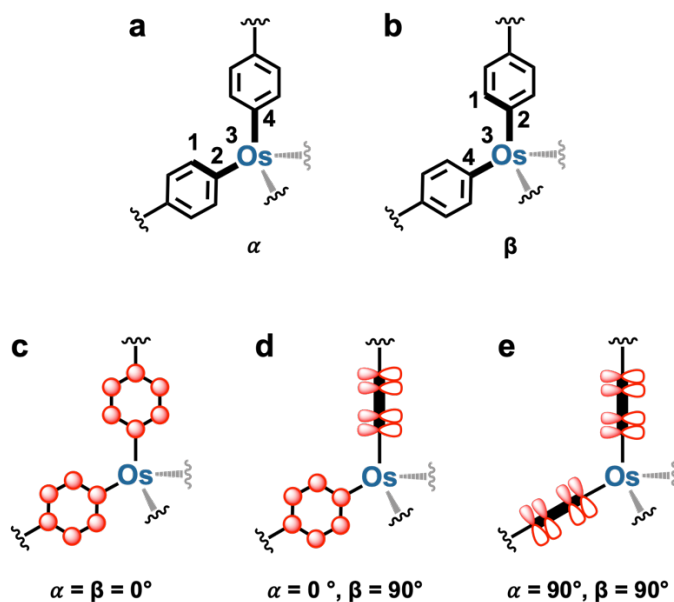


Figure S15. (a,b) The relative orientation of adjacent aryl ligands can be defined using two different dihedral angles, α and β . We define these angles using atoms 1-4, connected in each schematic through bonds with bold linewidths. In each case, atom 1 was chosen as the aryl carbon atom closest to the bond defined by atoms 3 and 4. (c-e) Illustrations of different aryl-aryl orientations, highlighting how they may influence overlap/coupling between each aryl π -system, at selected values of α and β .

All tetraaryl compounds comprise, by definition, four aryl groups we can label as *i*, *ii*, *iii*, and *iv*. These can be paired in six unique combinations – *i-ii*, *i-iii*, *i-iv*, *ii-iii*, *ii-iv*, and *iii-iv* – as illustrated in **Figure S16**. As such, any given compound has six pairs of dihedral angles (α and β ; 12 angles total).

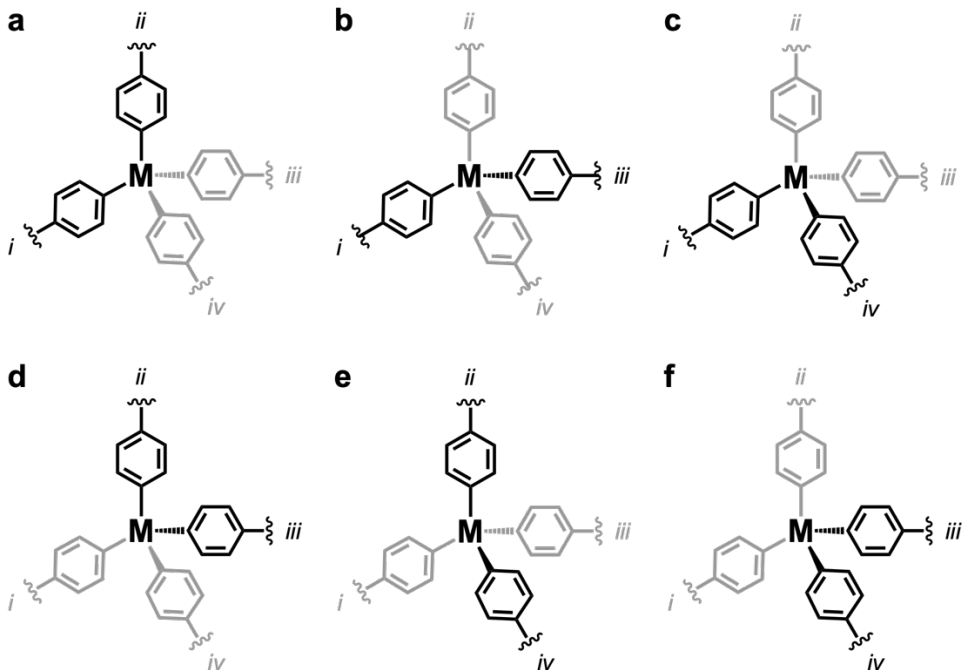


Figure S16. All tetraaryl compounds exhibit six pairs of dihedral angles, α and β (as defined in **Figure S15**). Each pair of angles is associated with one of the six unique combinations of aryl ligands – (a) $i\text{-}ii$, (b) $i\text{-}iii$, (c) $i\text{-}iv$, (d) $ii\text{-}iii$, (e) $ii\text{-}iv$, and (f) $iii\text{-}iv$ – illustrated schematically here.

In **Table S4** we present calculated sets of dihedral angle pairs for a self-consistent series of tetra(ferrocenylphenyl) compounds comprising Os(IV) (**Os-Fc**), C (**C-Fc**), or Si (**Si-Fc**) centers, structurally characterized through single-crystal X-ray diffraction.⁴ In **Table S5** we also present sets of dihedral angle pairs calculated for parent compounds with the ferrocenyl substituents removed, after optimizing their geometry using computational methods (Q-Chem). For each compound analyzed, we find that two dihedral pairs are *similar* ($\alpha \approx \beta$) and four are *different* ($\alpha \neq \beta$); denoted with black or blue text in the tables, respectively. Notably, the geometry where the angles are *different* approximates the one shown in **Figure S15d**, in which one angle is typically larger than $|61^\circ|$ and the other smaller than $|28^\circ|$. For geometries where the angles are *similar*, both angles lie between $|36^\circ|$ and $|58^\circ|$.

Table S4. Dihedral angles defining relative aryl ligand orientation in model tetraaryl compounds.^a

		dihedral angle pair					
		1	2	3	4	5	6
Os-Fc		-19.57	76.22	-42.26	-42.26	19.57	-76.22
Si-Fc		-64.54	28.21	54.58	54.58	-0.34	85.00
C-Fc		-0.57	-71.47	66.61	-5.19	-53.94	-48.28

^a All values in degrees, obtained from a self-consistent set of X-ray crystal structures of ferrocene-appended tetraaryl complexes.⁴ Blue angles = *different* dihedral angles in the pair, black = *similar* dihedral angles.

Table S5. Dihedral angles defining relative aryl ligand orientation in tetraaryl compounds after geometry optimization (Q-Chem).^a

		dihedral angle pair					
		1	2	3	4	5	6
Os(C ₈ H ₉) ₄		-57.16	-58.43	62.73	2.33	-61.72	-0.74
Si(C ₈ H ₉) ₄ ^b		-49.93	-50.40	70.03	-7.62	-70.26	6.94
Si(C ₆ H ₅) ₄		-37.84	-37.84	82.28	-24.51	-82.28	24.51
Si(C ₈ H ₉) ₄ ^c		-50.28	-50.28	70.19	-5.79	-70.08	5.73
C(C ₆ H ₅) ₄		64.75	1.52	-64.75	-1.52	-56.67	-56.67

^a All values in degrees, obtained following geometry optimization of parent compounds (unfunctionalized aryl ligands), based on X-ray crystal structures obtained by different groups,^{2,14,15} using PBE. Here both Si(C₆H₅)₄ and C(C₆H₅)₄ were optimized with S₄ symmetry, Si(C₈H₉)₄ (from the Si(C₆H₅)₄ starting geometry, green shaded entry) was optimized with C₂ symmetry. Ligands: C₆H₅ = phenyl; C₈H₉ = 2,5-xylyl. Blue angles = *different* dihedral angles in the pair, black = *similar* dihedral angles. ^b The optimized geometry of Si(C₈H₉)₄ (red shaded entry) was obtained from an input structure based on the optimized geometry of Os(C₈H₉)₄, after replacing the osmium atom for a silicon atom and adjusting all Si-aryl bonds to 1.9 Å. To facilitate the clearest comparison, the same aryl groups in Os(C₈H₉)₄ and Si(C₈H₉)₄ were used to calculate each of the dihedral angle pairs 1-6. ^c The optimized geometry of Si(C₈H₉)₄ (green shaded entry) was obtained from an input structure based on the optimized geometry of Si(C₆H₅)₄, after replacing selected aryl-H substituents for -CH₃. Similar dihedral angle pairs are obtained for Si(C₈H₉)₄ structures after geometry optimization from different input structures (shaded entries).

Significant differences in dihedral angle pairs are observed when reoptimizing the geometry of $\text{Si}(\text{C}_6\text{H}_5)_4$ after addition of $-\text{CH}_3$ groups to the 2- and 5-positions of the aryl rings to form $\text{Si}(\text{C}_8\text{H}_9)_4$ (**Table S5**, shaded entries). As changes in the equilibrium geometries and dihedral angle pairs of these species are expected to influence junction conductance (see discussion below), we note that in the present study we strictly compare the properties of compounds having Os–2,5-xylyl, Si–phenyl, and C–phenyl central fragments, rather than probing the influence of the tetrahedrally-coordinated central atoms alone.

In the **Tunnel Coupling (Q-Chem)** section below, we perform model calculations of wires connected to single gold atoms to help evaluate the extent to which these different classes of angle pairs – *similar* or *different* – influence electronic coupling between the π -systems of the associated aryl groups. In the **Additional Quantum Transport Calculations Data (FHI-aims)** section, we further evaluate how these aryl-aryl dihedral angle pairs modulate the calculated through-molecule transmission in wires connected to extended gold electrodes. These analyses reveal specific challenges associated with applying frozen geometries to calculate conductance trends for these systems.

Tunnel Coupling (Q-Chem)

We explored the properties of two sets of each model complex, **Os1h**, **Si1h**, and **C1h**. One set exhibited a pair of aryl substituents that had *similar* pairs of dihedral angles, and the other set had angles pairs that were *different* (see *Geometric Analysis*, above). The process of constructing each model essentially involved adding two $-\text{SMe}$ groups on different aryl substituents of the parent complex. In **Table S6** and **Table S7**, we present selected computational data for these model compounds obtained using the PBE and B3LYP functionals, respectively, both before and after adding Au_1 clusters.

We find that the HOMO-LUMO gap of each molecular complex does not strongly depend on whether the dihedral angle pair chosen is *similar* or *different*. This is rationalized given that this gap is a property of the entire molecule, and that the addition of $-\text{SMe}$ substituents to different aryl rings of each molecule simply generates geometric isomers with very similar electronic structures. Here we observe the same trends in HOMO-LUMO gap as found using FHI-aims (**Table S8**). The gaps are always smaller for **Os1h** than for **Si1h/C1h**, and the gaps are larger for

all models when using the B3LYP functional compared to PBE. Example isosurface plots for the frontier orbitals of each model are presented in **Figure S17,18**.

We use these models, now connected to Au_1 clusters through the sulfur atom of their $-\text{SMe}$ substituents, to explore changes in their calculated tunnel couplings, $2t$. The square of this quantity has been found to be proportional to the molecular junction conductance.^{17,37} In agreement with our experimental conductance measurements for **Os2** and **Si2** in PC, and with the results of quantum transport calculations (below), we find the tunnel coupling for **Os1h-Au₁** is consistently larger than for **Si1h-Au₁** or **C1h-Au₁** (**Table S6, S7**). Notably, this difference is maximized when using the PBE functional, and tunnel couplings calculated using PBE are also more variable between models with *similar* or *different* dihedral angle pairs, relative to those with B3LYP. Representative isosurface plots for the tunnel coupled orbitals of **Os1h-Au₁** are provided in **Figure S19**. The differences in tunnel coupling observed for non-equivalent geometries in these simple models can be reproduced for **Os1h**, **Si1h**, and **C1h** in transmission calculations using the same molecular structures connected between larger gold electrodes (**Figure 23**).

Table S6. Selected computational data for **Os1h**, **Si1h**, **C1h** models using the PBE functional.^a

	s/d ^b	α (°) ^c	β (°) ^c	HOMO (eV)	LUMO (eV)	gap (eV) ^d	$4t^2$ (eV ²)
Os1h	s	54.9	57.1	-3.817	-2.222	1.595	-
	d	-64.2	-0.3	-3.813	-2.242	1.571	-
Si1h	s	-38.5	-38.5	-4.867	-1.271	3.596	-
	d	-83.7	25.8	-4.857	-1.276	3.581	-
C1h	s	59.3	59.3	-4.642	-1.144	3.498	-
	d	-72.9	9.4	-4.770	-1.284	3.487	-
Os1h-Au₁	s	49.5	50.6	-3.854	-3.741	-	1.3×10^{-2}
	d	-60.8	-4.0	-3.845	-3.728	-	1.4×10^{-2}
Si1h-Au₁	s	-47.1	-39.5	-3.971	-3.964	-	4.5×10^{-5}
	d	-80.1	39.4	-3.972	-3.949	-	5.3×10^{-4}
C1h-Au₁	s	64.8	64.0	-3.976	-3.903	-	5.4×10^{-3}
	d	-75.9	12.6	-3.943	-3.933	-	9.3×10^{-5}

^a Calculations performed as described in *Computational Details*. ^b Here, s/d = similar or different dihedral angles for the selected pair of aryls functionalized with -SMe groups. ^c Dihedral angles after geometry optimization. Note the same input geometry for each series (the parent molecule with appended -SMe groups, without Au₁ clusters) was used in the calculations here using PBE and those in **Table S7** using B3LYP. ^d Where gap = LUMO – HOMO.

Table S7. Selected computational data for **Os1h**, **Si1h**, **C1h** models using the B3LYP functional.^a

	s/d ^b	α (°) ^c	β (°) ^c	HOMO (eV)	LUMO (eV)	gap (eV) ^d	$4t^2$ (eV ²)
Os1h	s	56.7	56.2	-4.615	-1.675	2.940	-
	d	-64.8	0.5	-4.617	-1.692	2.925	-
Si1h	s	-38.8	-38.8	-5.641	-0.543	5.098	-
	d	-83.0	24.3	-5.629	-0.546	5.083	-
C1h	s	57.9	57.9	-5.404	-0.407	4.998	-
	d	-71.5	8.2	-5.542	-0.532	5.010	-
Os1h-Au₁	s	55.5	57.0	-4.064	-3.776	-	8.3×10^{-2}
	d	-55.5	-10.7	-4.090	-3.756	-	1.1×10^{-1}
Si1h-Au₁	s	-36.8	-37.0	-4.123	-3.895	-	5.2×10^{-2}
	d	-80.0	29.2	-4.166	-3.933	-	5.4×10^{-2}
C1h-Au₁	s	67.8	70.1	-4.174	-3.882	-	8.5×10^{-2}
	d	-74.7	13.0	-4.141	-3.909	-	5.4×10^{-2}

^a Calculations performed as described in *Computational Details*. ^b Here, s/d = similar or different dihedral angles for the selected pair of aryls functionalized with -SMe groups. ^c Dihedral angles after geometry optimization. Note the same input geometry for each series (the parent molecule with appended -SMe groups, without Au₁ clusters) was used in the calculations here using B3LYP and those in **Table S6** using PBE. ^d Where gap = LUMO – HOMO.

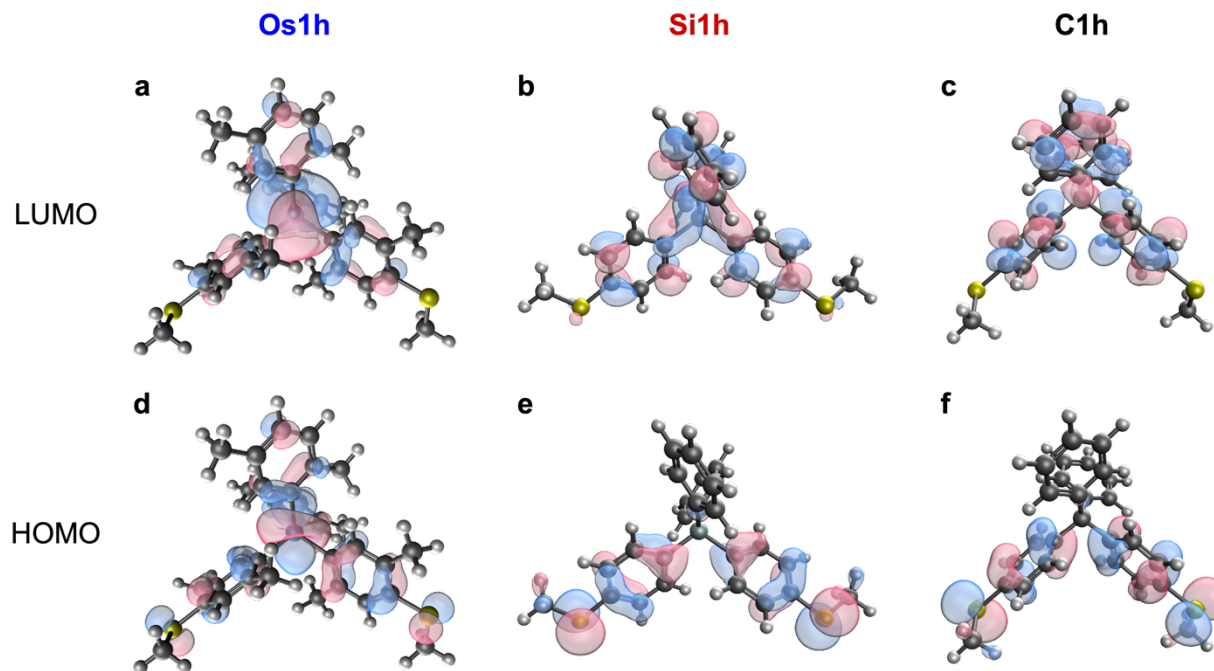


Figure S17. Isosurface plots of the **(a-c)** HOMO and **(d-e)** LUMO obtained from DFT calculations using B3LYP for gas phase **Os1**, **Si1**, and **C1** models (**Os1h**, **Si1h**, **C1h**, respectively; isovalue = 0.08 \AA^{-3} ; geometries correspond to those having similar dihedral angles for the selected pair of aryls functionalized with $-\text{SMe}$ groups). In each case, the HOMOs exhibit significant orbital density on the sulfur linkers, where the LUMOs do not, indicating these compounds should function as HOMO conductors. In **Os1h** there is a greater orbital density on the central atom (in this case, comprising an Os d_{z2} orbital rather than a C or Si sp^3 hybrid orbital). These plots corroborate the trends observed in the calculated transmission functions (**Figure 5b**) and suggest the increased conductance of **Os-n** relative to **Si-n** or **C-n** results from the extended delocalization of the thioanisole linker π -system across the central atom in the HOMO.

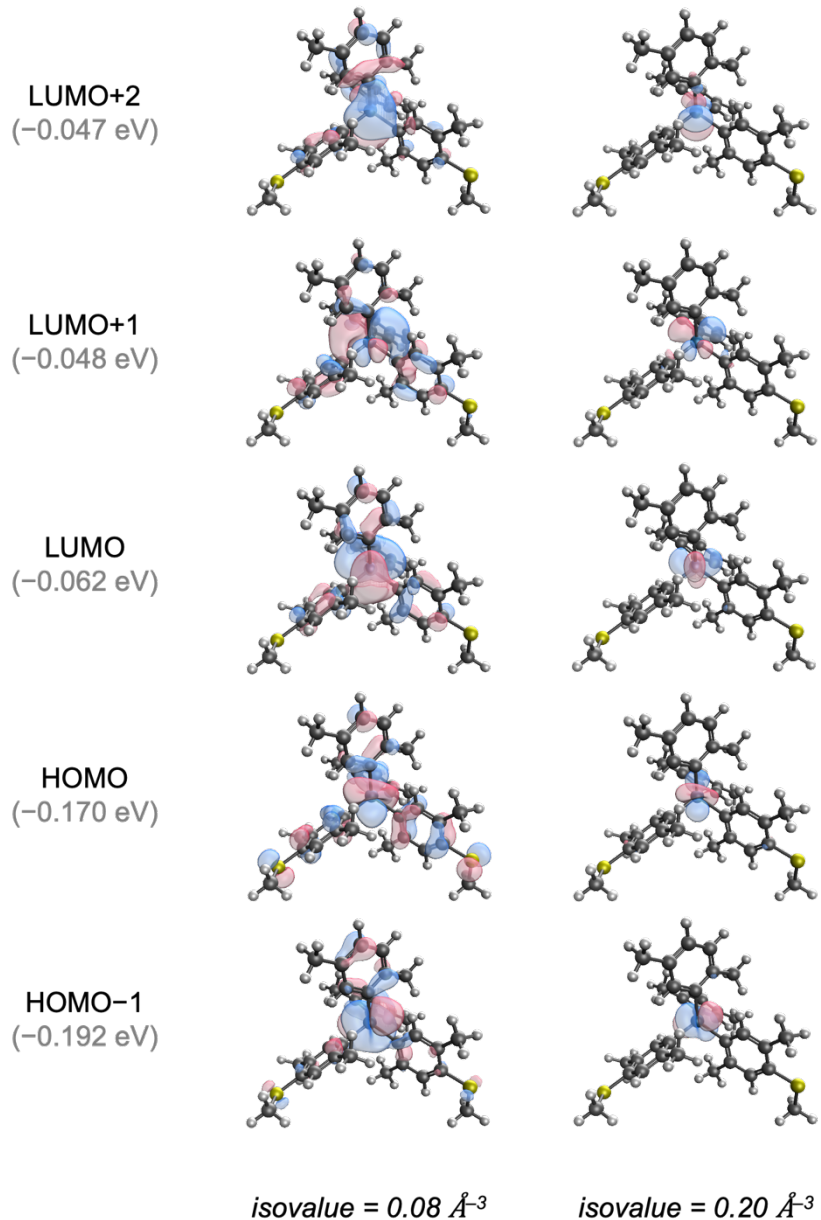


Figure S18. *Left:* Isosurface plots of an extended set of gas phase frontier orbitals for **Os1h** obtained from DFT calculations using B3LYP (isovalue = 0.08 Å⁻³; geometries correspond to those having similar dihedral angles for the selected pair of aryls functionalized with –SMe groups). HOMO and LUMO are reproduced from **Figure 17** for convenience. *Right:* The same isosurface plots calculated using isovalue = 0.20 Å⁻³ to help assign the *d*-orbital component of each molecular orbital. These results agree well with the expected electronic structure of such low spin *d*⁴ tetrahedral complexes, comprising frontier orbital sets of *e* (HOMO–1, HOMO) and *t*₂ (LUMO, LUMO+1, LUMO+2) symmetry.³⁸ Here, however, HOMO–1 (*d*_{x²–y²} character) and HOMO (*d*_{z²}) are non-degenerate, and the LUMO (*d*_{xy}) lies at a lower energy than LUMO+1 and LUMO+2 (*d*_{xz}, *d*_{yz}). We attribute the broken degeneracy of each set to the distorted coordination environment,⁵ and the asymmetric ligand field of this heteroleptic model complex.

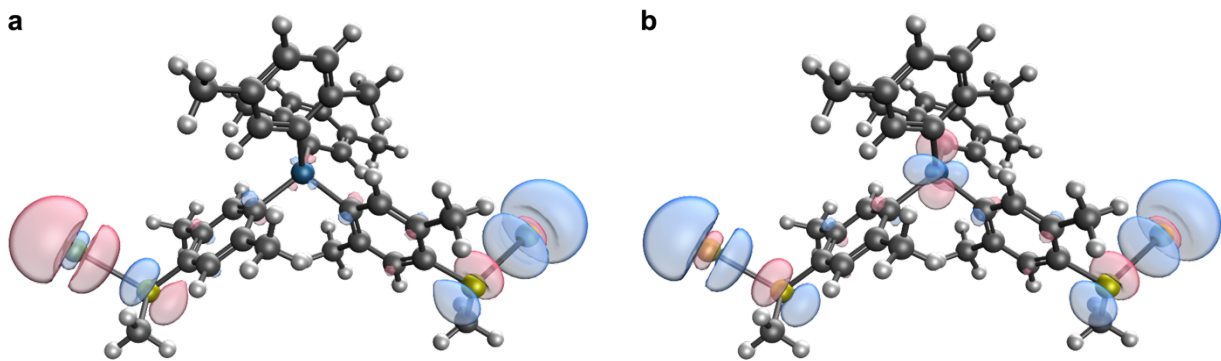


Figure S19. Isosurface plots of the (a) HOMO (antisymmetric) and (b) LUMO (symmetric) frontier orbitals obtained from DFT calculations using B3LYP for a **Os1** model (**Os1h**) bound to Au_1 clusters (isovalue = 0.08 \AA^{-3} ; geometries correspond to those having similar dihedral angles for the selected pair of aryls functionalized with $-\text{SMe}$ groups). These orbital plots are consistent with those observed in previous reports,^{37,39} and illustrate how the Au s orbitals are tunnel coupled through the tetrahedral bridge.

Additional Quantum Transport Calculations Data (FHI-aims)

Table S8. HOMO-LUMO gaps (in eV) for the **Os-*n***, **Si-*n***, and **C-*n*** molecular series, calculated using the PBE and B3LYP functionals. We employed the same DFT computational parameters as described in *Section: General Information of the SI*. These computational parameters converge the HOMO-LUMO gaps within a window of 20 meV.

compound	PBE (eV)	B3LYP (eV)
Os1	1.560	2.862
Os2	1.660	2.963
Os3	1.723	3.077
Si1	3.400	4.808
Si2	2.948	4.269
Si3	2.740	4.021
C1	3.246	4.660
C2	2.985	4.301
C3	2.761	4.038

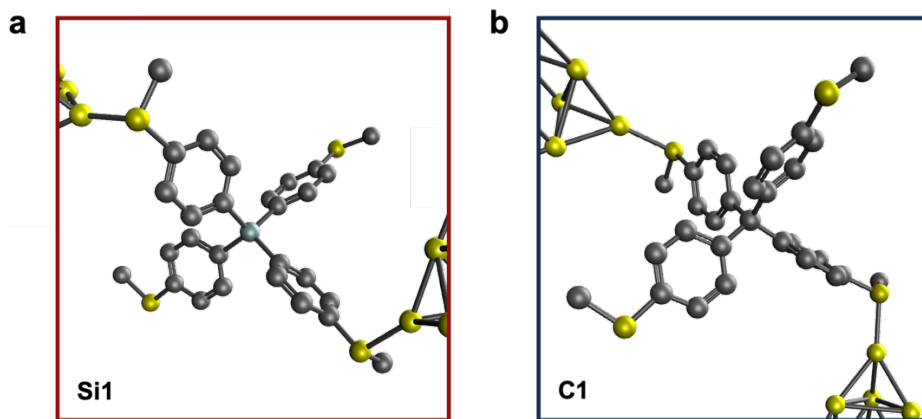


Figure S20. Additional representative junction geometries for (b) **Si1** and (c) **C1**. Hydrogen atoms excluded for clarity.

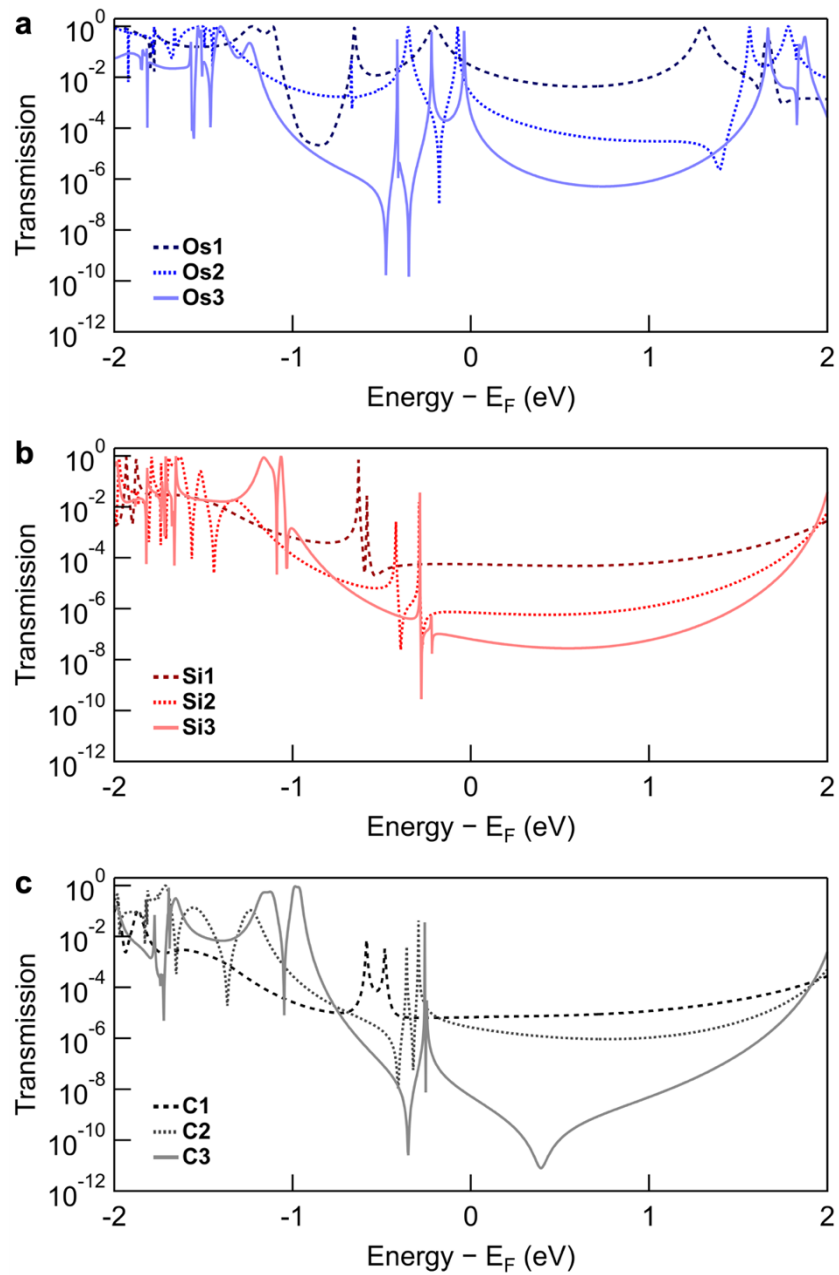


Figure S21. Overlaid calculated transmission functions for (a) **Os-*n***, (b) **Si-*n***, and (c) **C-*n***. Data for **Os-*n***, **Si2**, and **C2** are reproduced here from **Figure 5**, shown in an expanded format for clarity.

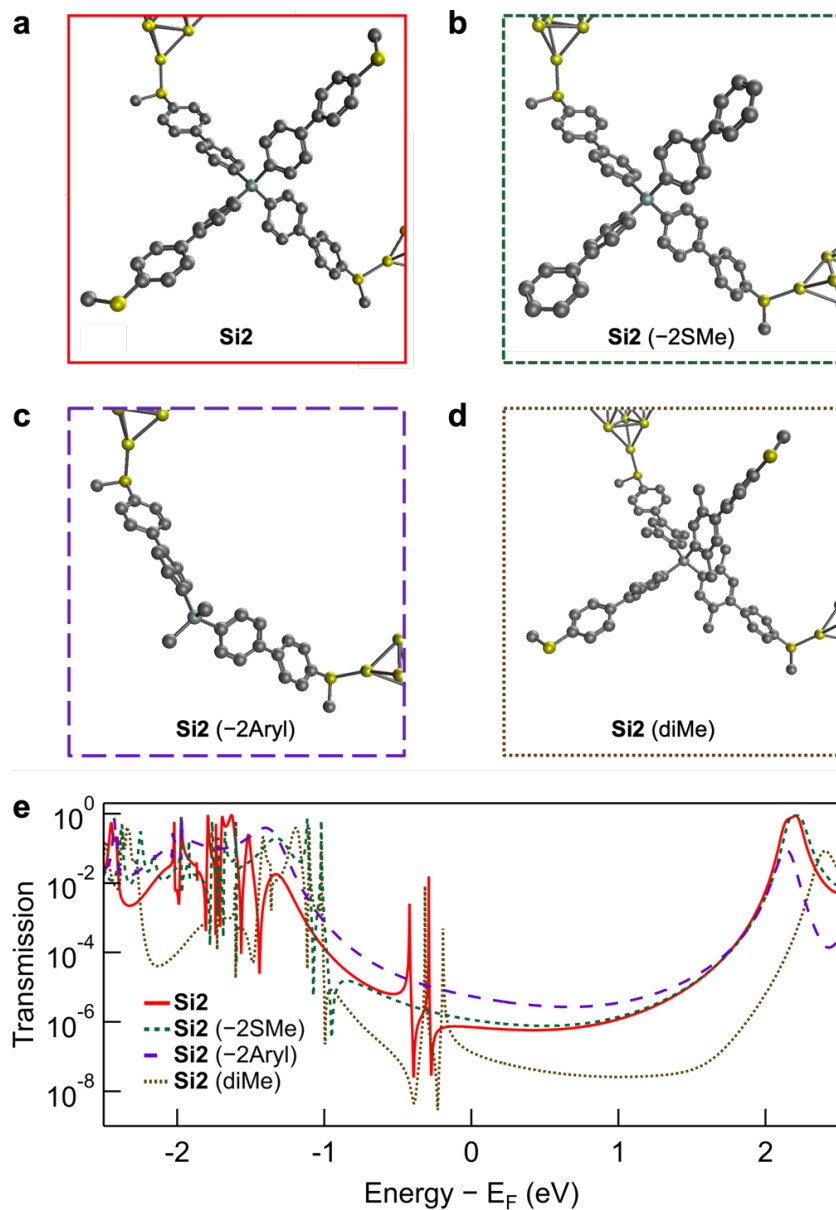


Figure S22. Junction geometries for: (a) **Si2**; (b) **-2SMe** and (c) **-2Aryl**, formed by removing thioether groups from unbound linker arms, or replacing the unbound arms of **Si2** with $-CH_3$ groups, respectively; (d) **diMe**, formed by adding $-CH_3$ groups in the 2- and 5-positions of each aryl connected to the silicon center of **Si2**. Hydrogen atoms excluded for clarity. Input structures from geometry optimization were constructed from the **Si2** junction shown in panel (a), to ensure the gold electrodes were connected to the same thioether linkers in each case. (e) Overlaid transmission functions for the junctions shown in panels (a-d). The data for **-2SMe** and **-2Aryl** junctions exhibit energetically shifted or completely absent Fano-type resonances, respectively. The transmission function for **diMe** junctions deviates from that of the parent **Si2** junction. Here, the electron-donating and bulky $-CH_3$ groups shift the LUMO resonance at ~ 2 eV to higher energy, also modulating the relative orientation/coupling between Si-connected aryl rings (**Table S5**). Junction geometry and transmission function for **Si2** reproduced from **Figure 5d** for convenience.

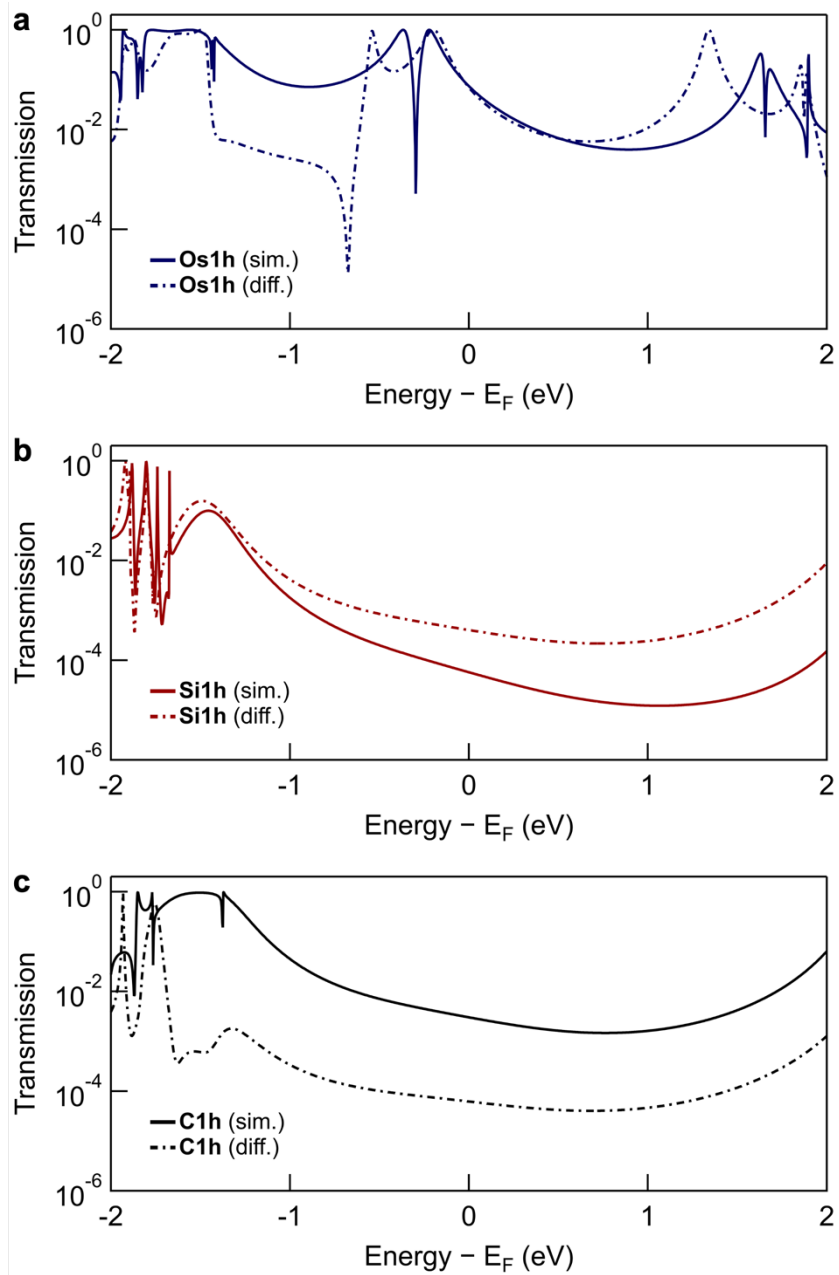


Figure S23. Transmission calculations for (a) Os1h, (b) Si1h, and (b) C1h junctions using the PBE functional, with electrodes connected at different $-SMe$ groups. Here, the same molecular geometries, having similar or different dihedral angles, were used as for the above tunnel coupling calculations. The trends in calculated transmission at E_F using larger gold cluster electrodes follow those identified with Au_1 clusters. This highlights the impact of aryl-central atom-aryl geometries on transport through these wires and shows that the results of isolated calculations using specific geometries must be interpreted with care. We stress again here that these aryl groups are expected to freely rotate at room temperature in solution, such that the experimentally measured conductance for **Os-n**, **Si-n**, and **C-n** junctions corresponds to a time-averaged sample of all energetically accessible geometries.

7. NMR Spectra

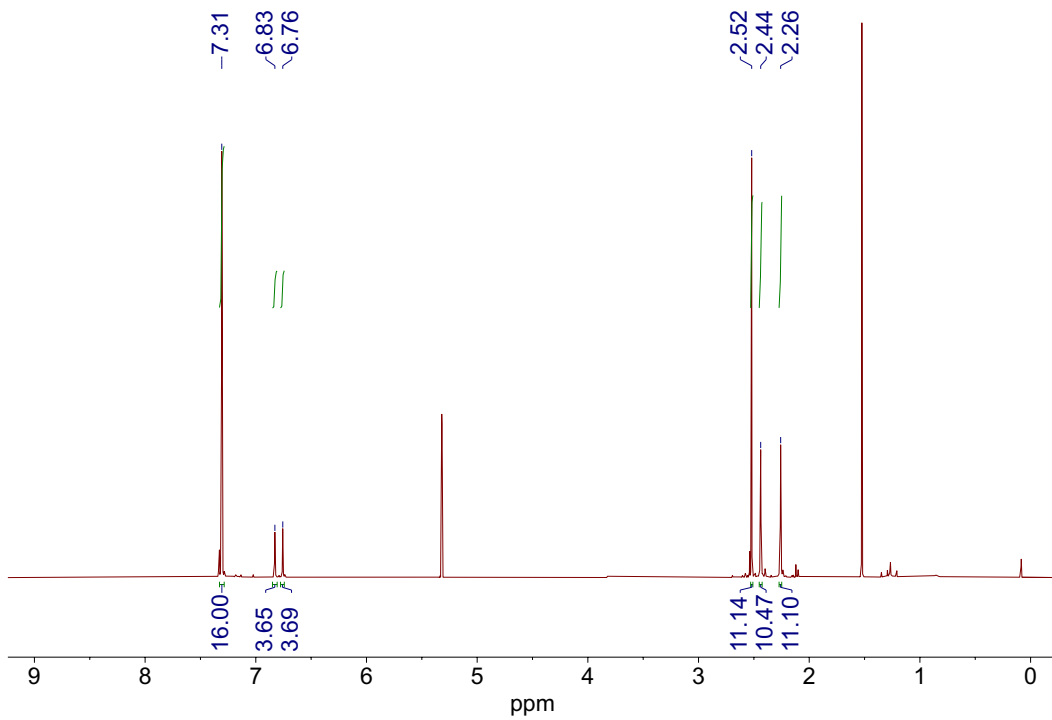


Figure S24. ^1H NMR (400 MHz) spectrum of **Os2** in CD_2Cl_2 .

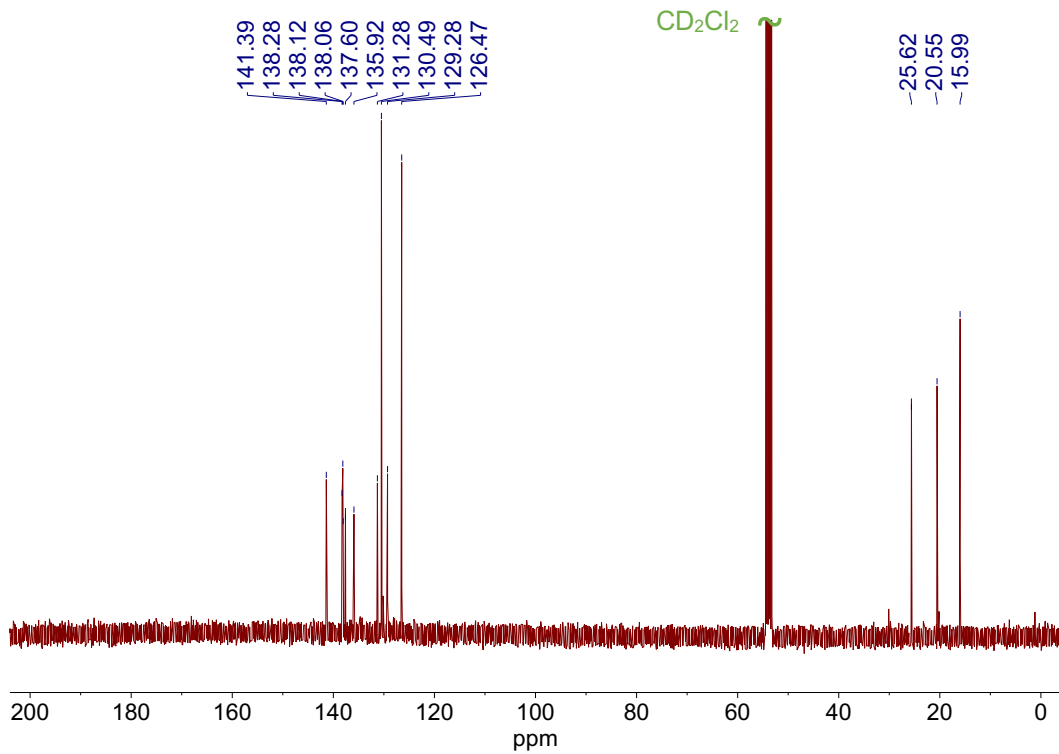


Figure S25. $^{13}\text{C}\{\text{H}\}$ NMR (100 MHz) spectrum of **Os2** in CD_2Cl_2 .

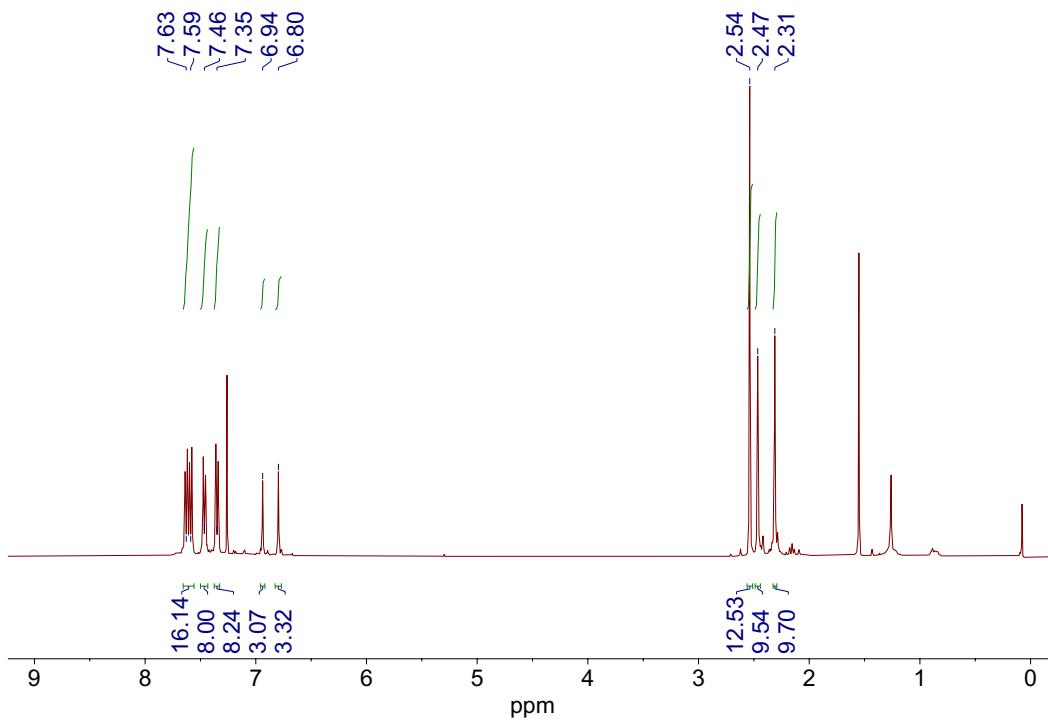


Figure S26. ^1H NMR (400 MHz) spectrum of **Os3** in CDCl_3 .

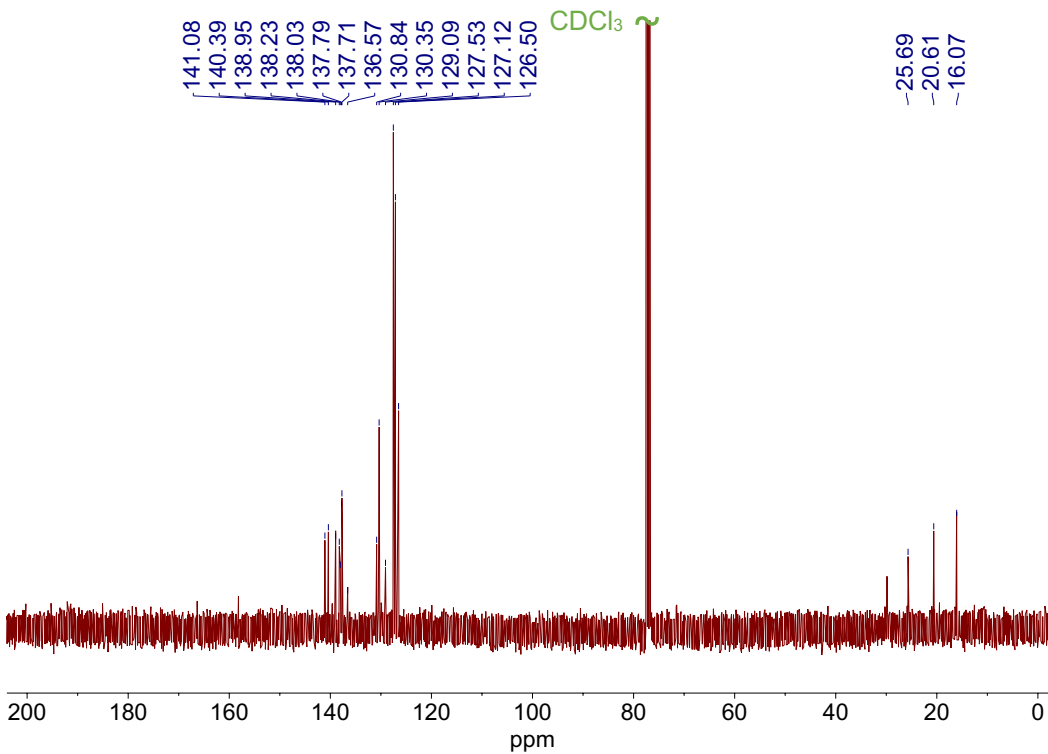


Figure S27. $^{13}\text{C}\{^1\text{H}\}$ NMR (101 MHz) spectrum of **Os3** in CDCl_3 .

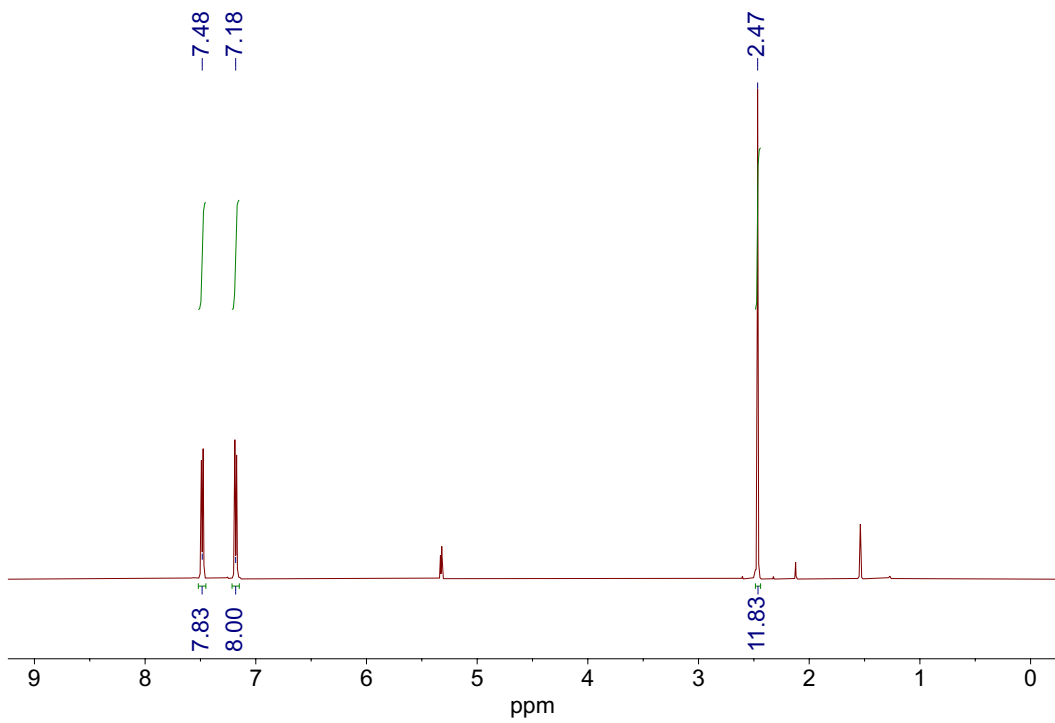


Figure S28. ^1H NMR (500 MHz) spectrum of **Si1** in CD_2Cl_2 .

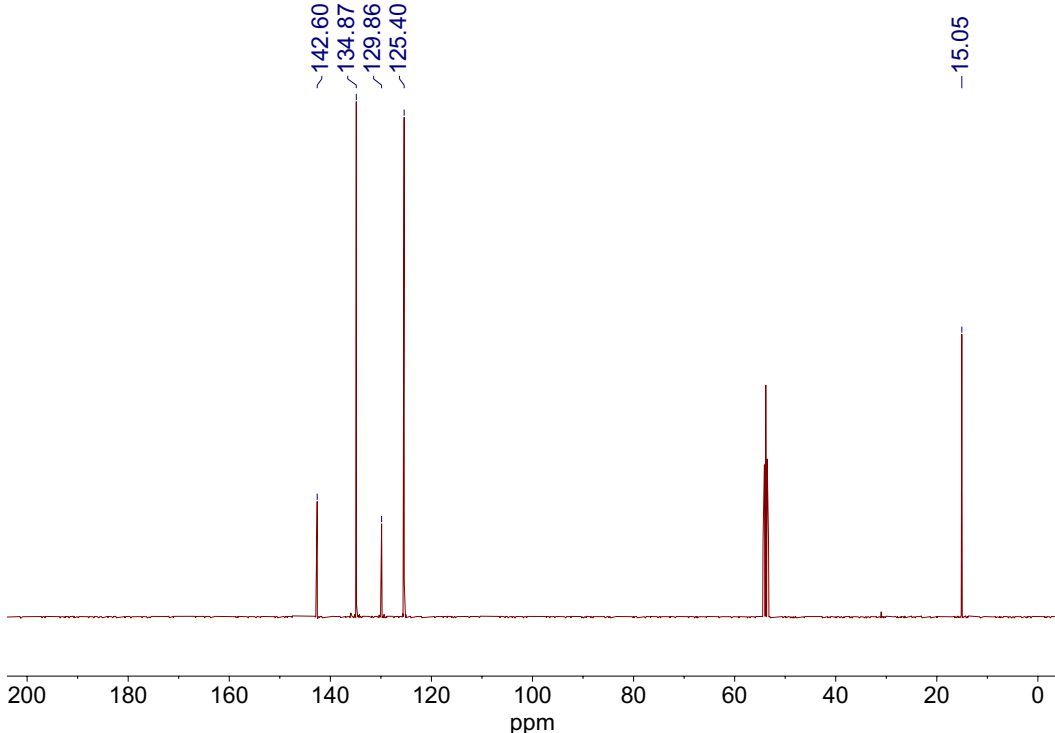


Figure S29. $^{13}\text{C}\{^1\text{H}\}$ NMR (101 MHz) spectrum of **Si1** in CD_2Cl_2 .

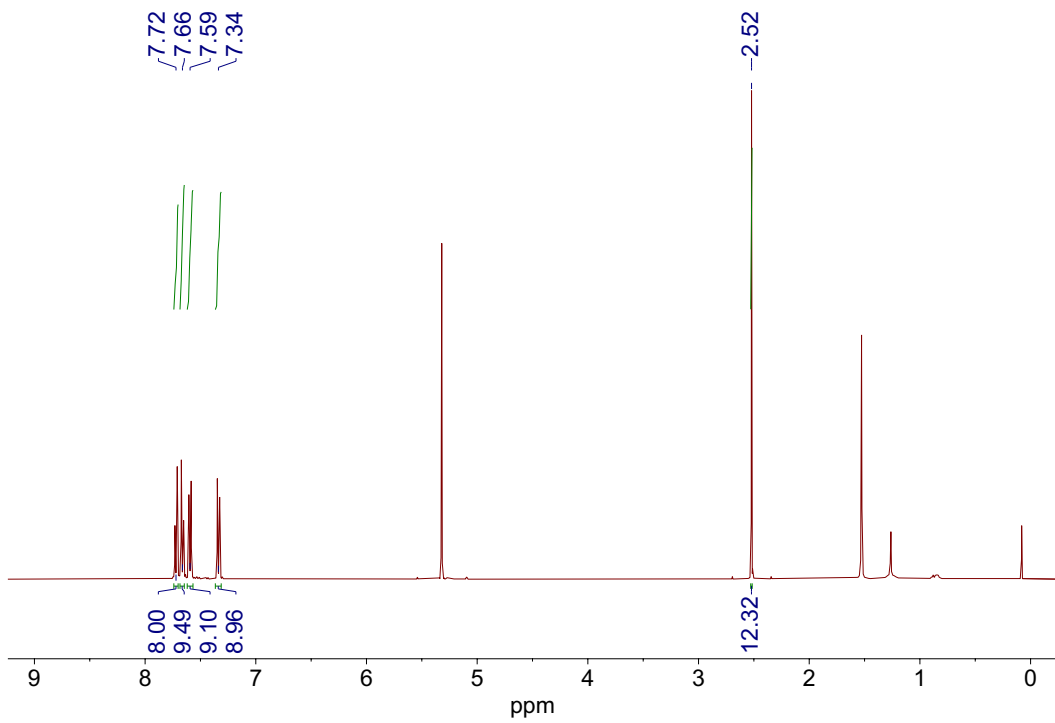


Figure S30. ^1H NMR (400 MHz) spectrum of **Si2** in CD_2Cl_2 .

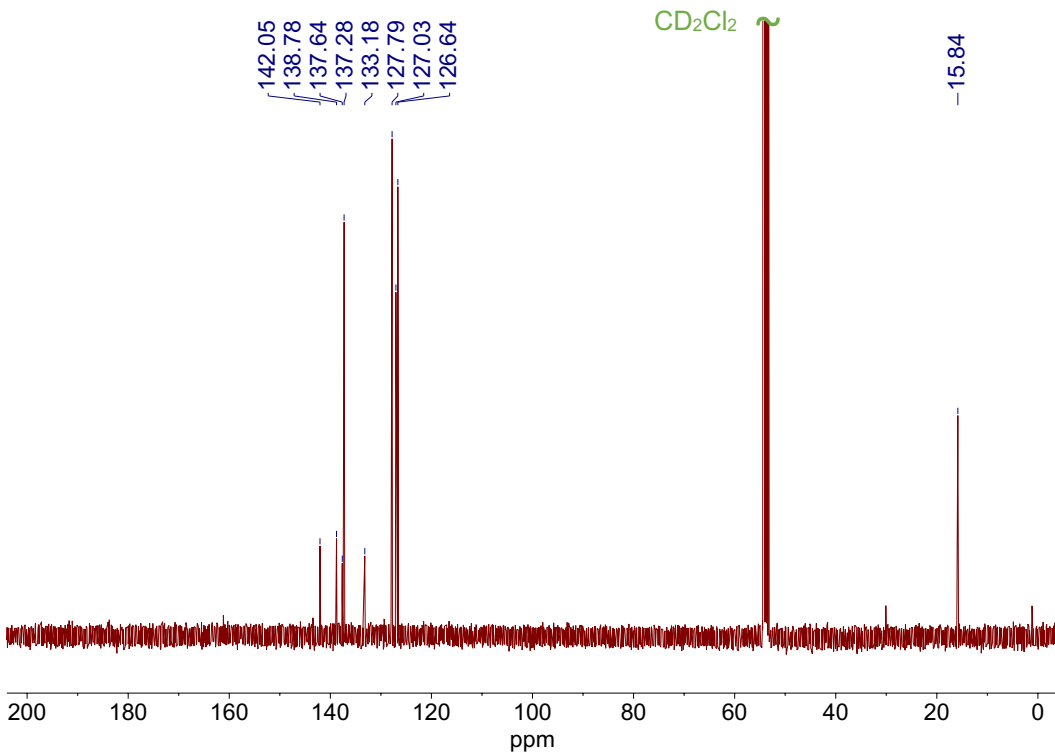


Figure S31. $^{13}\text{C}\{^1\text{H}\}$ NMR (101 MHz) spectrum of **Si2** in CD_2Cl_2 .

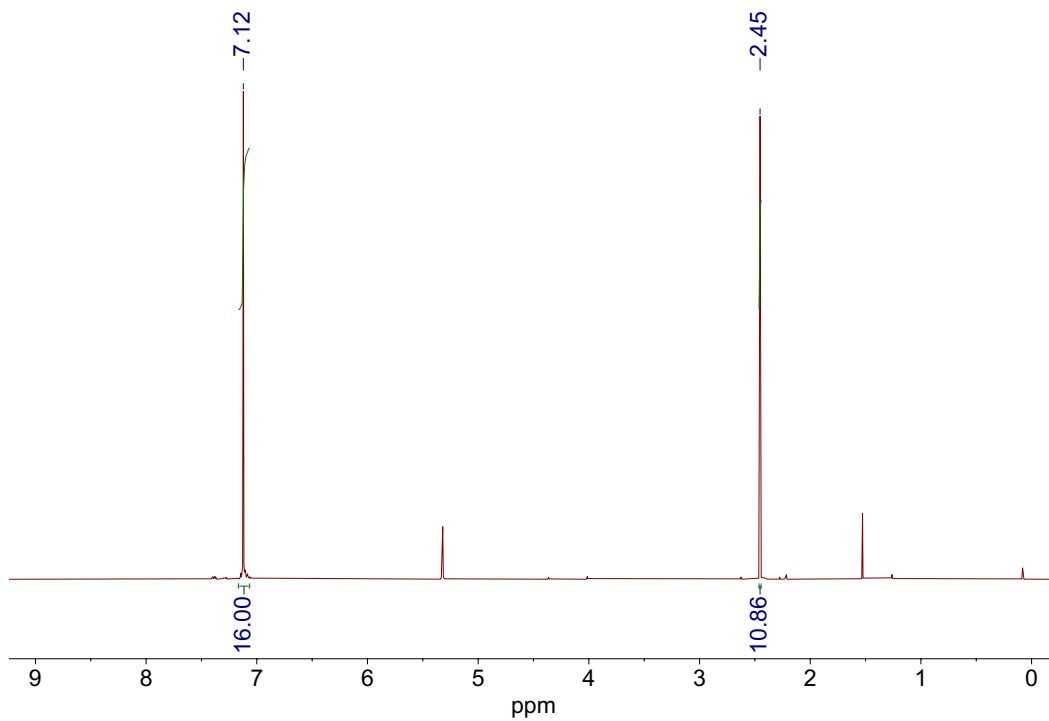


Figure S32. ^1H NMR (400 MHz) spectrum of **C1** in CD_2Cl_2 .

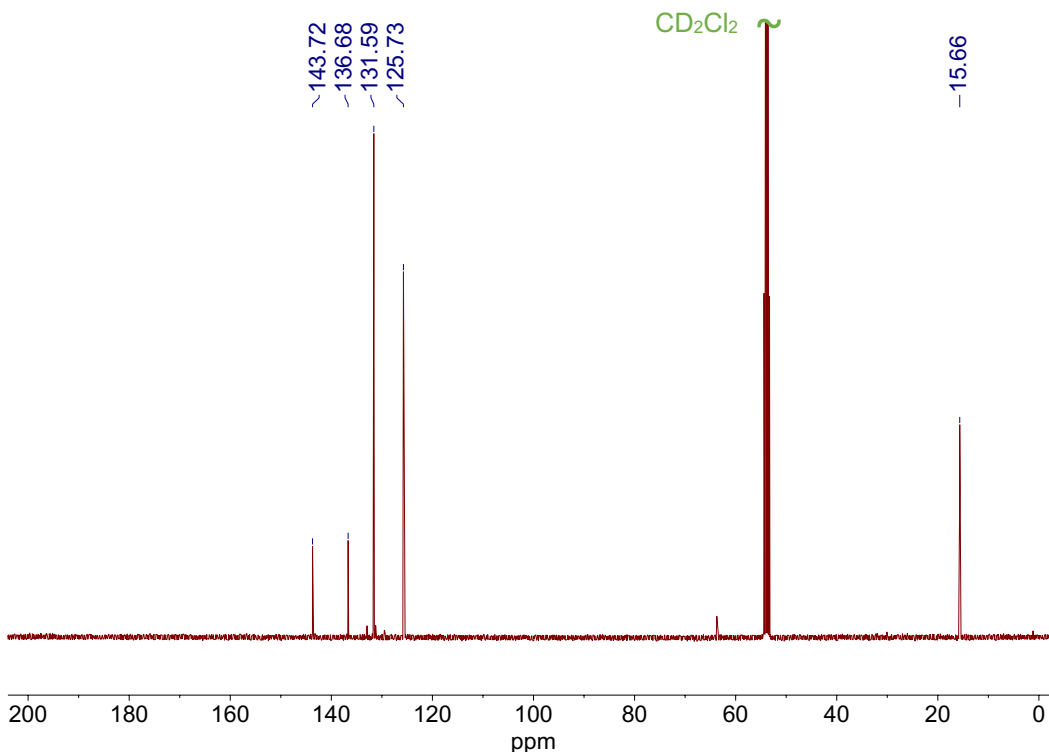


Figure S33. $^{13}\text{C}\{^1\text{H}\}$ NMR (150 MHz) spectrum of **C1** in CD_2Cl_2

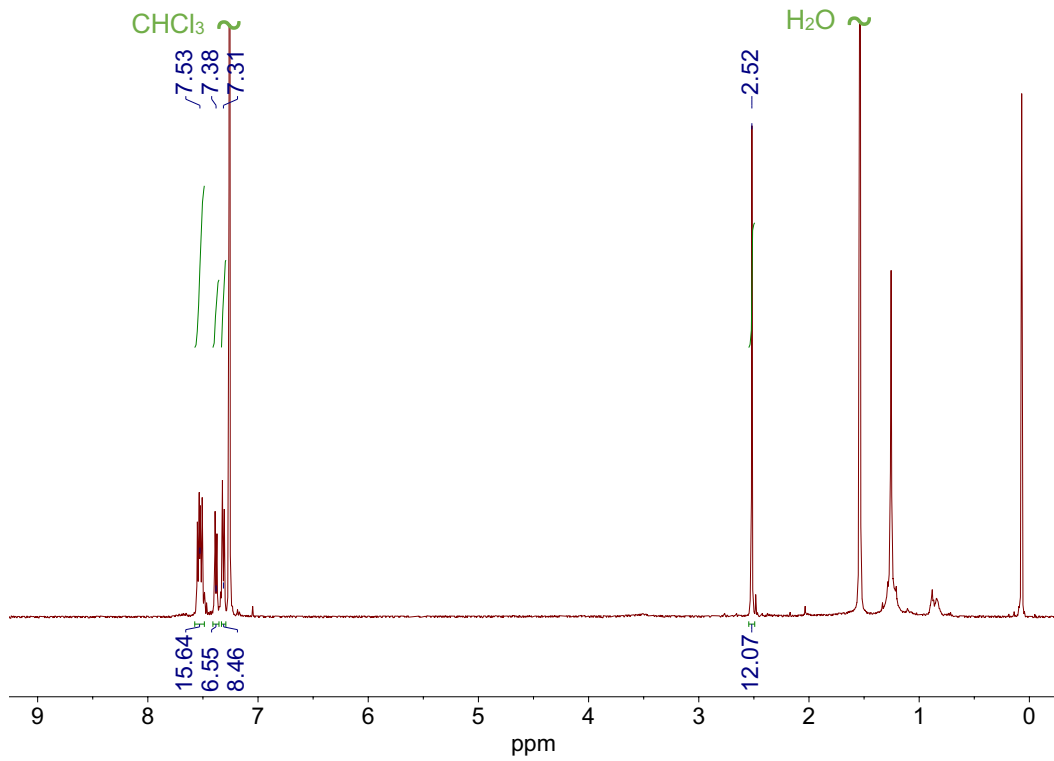


Figure S34. ¹H NMR (500 MHz) spectrum of C2 in CDCl₃.

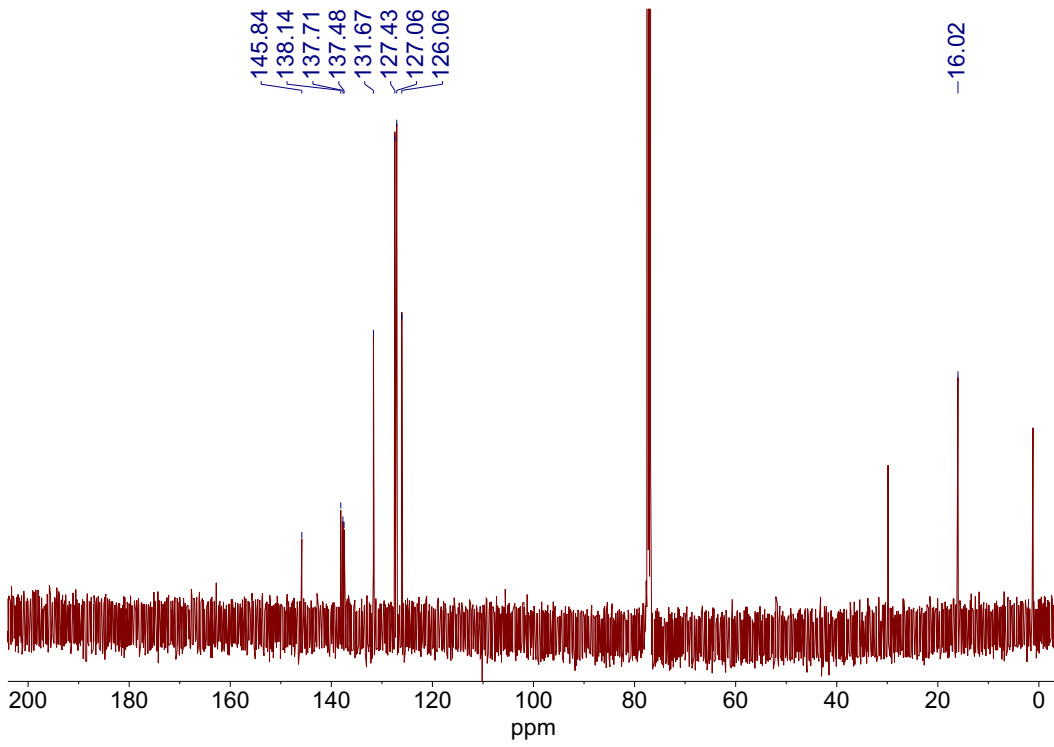


Figure S35. ¹³C{¹H} NMR (126 MHz) spectrum of C2 in CDCl₃.

7. References

- (1) Williams, D. B. G.; Lawton, M. Drying of Organic Solvents: Quantitative Evaluation of the Efficiency of Several Desiccants. *J. Org. Chem.* **2010**, *75* (24), 8351–8354.
- (2) Parr, J. M.; Olivari, C.; Saal, T.; Haiges, R.; Inkpen, M. S. Pushing Steric Limits in Osmium(Iv) Tetraaryl Complexes. *Dalton Trans.* **2022**, *51* (27), 10558–10570.
- (3) Love, B. E.; Jones, E. G. The Use of Salicylaldehyde Phenylhydrazone as an Indicator for the Titration of Organometallic Reagents. *J. Org. Chem.* **1999**, *64* (10), 3755–3756.
- (4) Zagami, L.; Saal, T.; Avedian, C.; Inkpen, M. S. Intervalence Charge Transfer in an Osmium(IV) Tetra(Ferrocenylaryl) Complex. *Inorg. Chem.* **2025**, *64* (5), 2312–2320.
- (5) Olivari, C.; Parr, J. M.; Avedian, C.; Saal, T.; Zagami, L.; Haiges, R.; Sharma, M.; Inkpen, M. S. Osmium(IV) Tetraaryl Complexes Formed from Prefunctionalized Ligands. *Inorg. Chem.* **2025**, *64* (12), 6192–6204.
- (6) Yang, J.; He, W.; Denman, K.; Jiang, Y. B.; Qin, Y. A Molecular Breakwater-like Tetrapod for Organic Solar Cells. *J. Mater. Chem. A* **2015**, *3* (5), 2108–2119.
- (7) Starr, R. L.; Fu, T.; Doud, E. A.; Stone, I.; Roy, X.; Venkataraman, L. Gold–Carbon Contacts from Oxidative Addition of Aryl Iodides. *J. Am. Chem. Soc.* **2020**, *142* (15), 7128–7133.
- (8) Fulmer, G. R.; Miller, A. J. M.; Sherden, N. H.; Gottlieb, H. E.; Nudelman, A.; Stoltz, B. M.; Bercaw, J. E.; Goldberg, K. I. NMR Chemical Shifts of Trace Impurities: Common Laboratory Solvents, Organics, and Gases in Deuterated Solvents Relevant to the Organometallic Chemist. *Organometallics* **2010**, *29* (9), 2176–2179.
- (9) Kim, L.; Czyszczon-Burton, T. M.; Nguyen, K. M.; Stukey, S.; Lazar, S.; Prana, J.; Miao, Z.; Park, S.; Chen, S. F.; Inkpen, M. S. Low Vapor Pressure Solvents for Single-Molecule Junction Measurements. *Nano Lett.* **2024**, *24* (32), 9998–10005.
- (10) Venkataraman, L.; Klare, J. E.; Tam, I. W.; Nuckolls, C.; Hybertsen, M. S.; Steigerwald, M. L. Single-Molecule Circuits with Well-Defined Molecular Conductance. *Nano Lett.* **2006**, *6*
- (11) Inkpen, M. S.; Liu, Z.; Li, H.; Campos, L. M.; Neaton, J. B.; Venkataraman, L. Non-Chemisorbed Gold–Sulfur Binding Prevails in Self-Assembled Monolayers. *Nat. Chem.* **2019**, *11*, 351–358.
- (12) Miao, Z.; Quainoo, T.; Czyszczon-Burton, T. M.; Rotthowe, N.; Parr, J. M.; Liu, Z.; Inkpen, M. S. Charge Transport across Dynamic Covalent Chemical Bridges. *Nano Lett.* **2022**, *22* (20), 8331–8338.
- (13) Epifanovsky, E.; Gilbert, A. T. B.; Feng, X.; Lee, J.; Mao, Y.; Mardirossian, N.; Pokhilko, P.; White, A. F.; Coons, M. P.; Dempwolff, A. L.; Gan, Z.; Hait, D.; Horn, P. R.; Jacobson, L. D.; Kaliman, I.; Kussmann, J.; Lange, A. W.; Lao, K. U.; Levine, D. S.; Liu, J.; McKenzie, S. C.; Morrison, A. F.; Nanda, K. D.; Plasser, F.; Rehn, D. R.; Vidal, M. L.; You, Z. Q.; Zhu, Y.; Alam, B.; Albrecht, B. J.; Aldossary, A.; Alguire, E.; Andersen, J. H.; Athavale, V.; Barton, D.; Begam, K.; Behn, A.; Bellonzi, N.; Bernard, Y. A.; Berquist, E. J.; Burton, H. G. A.; Carreras, A.; Carter-Fenk, K.; Chakraborty, R.; Chien, A. D.; Closser, K. D.; Cofer-Shabica, V.; Dasgupta, S.; De Wergifosse, M.; Deng, J.; Diedenhofen, M.; Do, H.; Ehlert, S.; Fang, P. T.; Fatehi, S.; Feng, Q.; Friedhoff, T.; Gayvert, J.; Ge, Q.; Gidofalvi, G.; Goldey, M.; Gomes, J.; González-Espinoza, C. E.; Gulania, S.; Gunina, A. O.; Hanson-Heine, M. W. D.; Harbach, P. H. P.; Hauser, A.; Herbst, M. F.; Hernández Vera, M.; Hodecker, M.; Holden, Z. C.; Houck, S.; Huang, X.; Hui, K.; Huynh, B. C.; Ivanov, M.; Jász, Á.; Ji, H.; Jiang, H.; Kaduk, B.; Kähler, S.; Khistyayev, K.; Kim, J.; Kis, G.; Klunzinger, P.; Koczor-Benda, Z.; Koh, J. H.; Kosenkov, D.; Koulias, L.; Kowalczyk, T.; Krauter, C. M.; Kue, K.; Kunitsa, A.;

- Kus, T.; Ladjánszki, I.; Landau, A.; Lawler, K. V.; Lefrancois, D.; Lehtola, S.; Li, R. R.; Li, Y. P.; Liang, J.; Liebenthal, M.; Lin, H. H.; Lin, Y. S.; Liu, F.; Liu, K. Y.; Loipersberger, M.; Luenser, A.; Manjanath, A.; Manohar, P.; Mansoor, E.; Manzer, S. F.; Mao, S. P.; Marenich, A. V.; Markovich, T.; Mason, S.; Maurer, S. A.; McLaughlin, P. F.; Menger, M. F. S. J.; Mewes, J. M.; Mewes, S. A.; Morgante, P.; Mullinax, J. W.; Oosterbaan, K. J.; Paran, G.; Paul, A. C.; Paul, S. K.; Pavošević, F.; Pei, Z.; Prager, S.; Proynov, E. I.; Rák, Á.; Ramos-Cordoba, E.; Rana, B.; Rask, A. E.; Rettig, A.; Richard, R. M.; Rob, F.; Rossomme, E.; Scheele, T.; Scheurer, M.; Schneider, M.; Sergueev, N.; Sharada, S. M.; Skomorowski, W.; Small, D. W.; Stein, C. J.; Su, Y. C.; Sundstrom, E. J.; Tao, Z.; Thirman, J.; Tornai, G. J.; Tsuchimochi, T.; Tubman, N. M.; Veccham, S. P.; Vydrov, O.; Wenzel, J.; Witte, J.; Yamada, A.; Yao, K.; Yeganeh, S.; Yost, S. R.; Zech, A.; Zhang, I. Y.; Zhang, X.; Zhang, Y.; Zuev, D.; Aspuru-Guzik, A.; Bell, A. T.; Besley, N. A.; Bravaya, K. B.; Brooks, B. R.; Casanova, D.; Chai, J. D.; Coriani, S.; Cramer, C. J.; Cserey, G.; Deprince, A. E.; Distasio, R. A.; Dreuw, A.; Dunietz, B. D.; Furlani, T. R.; Goddard, W. A.; Hammes-Schiffer, S.; Head-Gordon, T.; Hehre, W. J.; Hsu, C. P.; Jagau, T. C.; Jung, Y.; Klamt, A.; Kong, J.; Lambrecht, D. S.; Liang, W.; Mayhall, N. J.; McCurdy, C. W.; Neaton, J. B.; Ochsenfeld, C.; Parkhill, J. A.; Peverati, R.; Rassolov, V. A.; Shao, Y.; Slipchenko, L. V.; Stauch, T.; Steele, R. P.; Subotnik, J. E.; Thom, A. J. W.; Tkatchenko, A.; Truhlar, D. G.; Van Voorhis, T.; Wesolowski, T. A.; Whaley, K. B.; Woodcock, H. L.; Zimmerman, P. M.; Faraji, S.; Gill, P. M. W.; Head-Gordon, M.; Herbert, J. M.; Krylov, A. I. Software for the Frontiers of Quantum Chemistry: An Overview of Developments in the Q-Chem 5 Package. *J. Chem. Phys.* **2021**, *155*, 084801.
- (14) Robbins, A.; Jeffrey, G. A.; Chesick, J. P.; Donohue, J.; Cotton, F. A.; Frenz, B. A.; Murillo, C. A. A Refinement of the Crystal Structure of Tetraphenylmethane: Three Independent Redeterminations. *Acta Crystallogr. B* **1975**, *31* (10), 2395–2399.
 - (15) Gruhnert, V.; Kirfel, A.; Will, G.; Wallrafen, F.; Recker, K. The Crystal Structure and Electron Density of Tetraphenyl-Silicon, $(C_6H_5)_4Si$. *Z. Krist.* **1983**, *163*, 53–60.
 - (16) Woitellier, S.; Launay, J. P.; Joachim. The Possibility of Molecular Switching: Theoretical Study of $[(NH_3)_5Ru-4,4'-Bipy-Ru(NH_3)_5]^{5+}$. *Chem. Phys.* **1989**, *131*, 481–488.
 - (17) Venkataraman, L.; Klare, J. E.; Nuckolls, C.; Hybertsen, M. S.; Steigerwald, M. L. Dependence of Single-Molecule Junction Conductance on Molecular Conformation. *Nature* **2006**, *442* (7105), 904–907.
 - (18) Blum, V.; Gehrke, R.; Hanke, F.; Havu, P.; Havu, V.; Ren, X.; Reuter, K.; Scheffler, M. Ab Initio Molecular Simulations with Numeric Atom-Centered Orbitals. *Comput. Phys. Commun.* **2009**, *180* (11), 2175–2196.
 - (19) Perdew, J. P.; Burke, K.; Ernzerhof, M. Generalized Gradient Approximation Made Simple. *Phys. Rev. Lett.* **1996**, *77* (18), 3865–3868.
 - (20) Lenthe, E. V.; Baerends, E. J.; Snijders, J. G. Relativistic Regular Two-Component Hamiltonians. *J. Chem. Phys.* **1993**, *99* (6), 4597–4610.
 - (21) Camarasa-Gómez, M.; Hernández-Pérez, D.; Evers, F. Spin–Orbit Torque in Single-Molecule Junctions from Ab Initio. *J. Phys. Chem. Lett.* **2024**, *15* (21), 5747–5753.
 - (22) Arnold, A.; Weigend, F.; Evers, F. Quantum Chemistry Calculations for Molecules Coupled to Reservoirs: Formalism, Implementation, and Application to Benzenedithiol. *J. Chem. Phys.* **2007**, *126* (17), 174101.
 - (23) Bagrets, A. Spin-Polarized Electron Transport Across Metal–Organic Molecules: A Density Functional Theory Approach. *J. Chem. Theory Comput.* **2013**, *9* (6), 2801–2815.

- (24) Lau, M.-K.; Zhang, Q.-F.; Chim, J. L. C.; Wong, W.-T.; Leung, W.-H. Direct Functionalisation of σ -Aryl Ligands: Preparation of Homoleptic Functionalised Aryls of Osmium(Iv). *Chem. Commun.* **2001**, *79* (16), 1478–1479.
- (25) Doud, E. A.; Inkpen, M. S.; Lovat, G.; Montes, E.; Paley, D. W.; Steigerwald, M. L.; Vázquez, H.; Venkataraman, L.; Roy, X. In Situ Formation of N-Heterocyclic Carbene-Bound Single-Molecule Junctions. *J. Am. Chem. Soc.* **2018**, *140* (28), 8944–8949.
- (26) Lau, M.-K. Transition Metal Complexes with Functionalized Aryl Ligands, Hong Kong University of Science and Technology, 1999.
- (27) Liu, X.-M.; He, C.; Xu, J.-W. Synthesis and Optical Properties of Tetraphenylmethane-Based Tetrahedral Fluorescent Compounds and Their Water-Soluble PEG-Linked Polymers. *Tetrahedron Lett.* **2004**, *45* (8), 1593–1597.
- (28) Liu, X.-M.; He, C.; Huang, J.; Xu, J. Highly Efficient Blue-Light-Emitting Glass-Forming Molecules Based on Tetraarylmethane/Silane and Fluorene: Synthesis and Thermal, Optical, and Electrochemical Properties. *Chem. Mater.* **2005**, *17* (2), 434–441.
- (29) Cheng, Z. L.; Skouta, R.; Vazquez, H.; Widawsky, J. R.; Schneebeli, S.; Chen, W.; Hybertsen, M. S.; Breslow, R.; Venkataraman, L. In Situ Formation of Highly Conducting Covalent Au-C Contacts for Single-Molecule Junctions. *Nat Nanotechnol.* **2011**, *6* (6), 353–357.
- (30) Li, Y.; Zhao, C.; Wang, R.; Tang, A.; Hong, W.; Qu, D.; Tian, H.; Li, H. In Situ Monitoring of Transmetallation in Electric Potential-Promoted Oxidative Coupling in a Single-Molecule Junction. *CCS Chem.* **2022**, *5*, 191–199.
- (31) Fatemi, V.; Kamenetska, M.; Neaton, J. B.; Venkataraman, L. Environmental Control of Single-Molecule Junction Transport. *Nano Lett.* **2011**, *11* (5), 1988–1992.
- (32) Dalmieda, J.; Shi, W.; Li, L.; Venkataraman, L. Solvent-Mediated Modulation of the Au–S Bond in Dithiol Molecular Junctions. *Nano Lett.* **2024**, *24* (2), 703–707.
- (33) Zang, Y.; Zou, Q.; Fu, T.; Ng, F.; Fowler, B.; Yang, J.; Li, H.; Steigerwald, M. L.; Nuckolls, C.; Venkataraman, L. Directing Isomerization Reactions of Cumulenes with Electric Fields. *Nat. Commun.* **2019**, *10* (1), 4482.
- (34) Prana, J.; Zagami, L.; Yan, K.; Hernangómez-Pérez, D.; Camarasa-Gómez, M.; Inkpen, M. S. Forming Chemisorbed Single-Molecule Junctions through Loss of Stable Carbocations. *Nano Lett.* **2025**, *25* (26), 10427–10434.
- (35) Prindle, C. R.; Shi, W.; Li, L.; Jensen, J. D.; Laursen, B. W.; Steigerwald, M. L.; Nuckolls, C.; Venkataraman, L. Effective Gating in Single-Molecule Junctions through Fano Resonances. *J. Am. Chem. Soc.* **2024**, *146* (3646–3650).
- (36) Bard, A. J.; Faulkner, L. Y. *Electrochemical Methods*; Wiley, 2004.
- (37) Venkataraman, L.; Park, Y. S.; Whalley, A. C.; Nuckolls, C.; Hybertsen, M. S.; Steigerwald, M. L. Electronics and Chemistry: Varying Single-Molecule Junction Conductance Using Chemical Substituents. *Nano Lett.* **2007**, *7* (2), 502–506.
- (38) Gray, H. B. Molecular Orbital Theory for Transition Metal Complexes. *J. Chem. Educ.* **1964**, *41* (1), 2.
- (39) Prana, J.; Kim, L.; Czyszczon-Burton, T.; Homann, G.; Chen, S.; Miao, Z.; Camarasa-Gómez, M.; Inkpen, M. Lewis-Acid Mediated Reactivity in Single-Molecule Junctions. *J. Am. Chem. Soc.* **2024**, *146* (48), 33265–33275.